UC Berkeley

UC Berkeley Previously Published Works

Title

Multivariate MR biomarkers better predict cognitive dysfunction in mouse models of Alzheimer's disease

Permalink

https://escholarship.org/uc/item/9pm6x6mf

Authors

Badea, Alexandra
Delpratt, Natalie A
Anderson, RJ
et al.

Publication Date

2019-07-01

DOI

10.1016/j.mri.2019.03.022

Peer reviewed

eScholarship.org Powered by the California Digital Library
University of California

Author Manuscript

Author Manuscript

Author Manuscript

Author Manuscript

HHS Public Access

Author manuscript

Magn Reson Imaging. Author manuscript; available in PMC 2020 July 01.

Published in final edited form as:

Magn Reson Imaging. 2019 July ; 60: 52–67. doi:10.1016/j.mri.2019.03.022.

Multivariate MR Biomarkers Better Predict Cognitive Dysfunction in Mouse Models of Alzheimer's Disease

Alexandra Badea[1,2,3,*], **Natalie A Delpratt**[1,*], **RJ Anderson**[1], **Russell Dibb**[1], **Yi Qi**[1], **Hongjiang Wei**[4], **Chunlei Liu**[5], **William C Wetsel**[6], **Brian B Avants**[7], **Carol Colton**[2]

[1]Center for In Vivo Microscopy, Department of Radiology, Duke University Medical Center, Durham NC

[2]Department of Neurology, Duke University Medical Center, Durham NC

[3]Brain Imaging and Analysis Center, Duke University, Durham, NC.

[4]Institute for Medical Imaging Technology, School of Biomedical Engineering, Shanghai Jiao Tong University, Shanghai, China

[5]Department of Electrical Engineering and Computer Science, University of California, Berkeley, CA

[6]Department of Psychiatry and Behavioral Sciences, Cell Biology, Neurobiology, Duke University Medical Center, Durham, NC

[7]Department of Radiology and Medical Imaging, University of Virginia, Charlottesville, VA

Abstract

To understand multifactorial conditions such as Alzheimer's disease (AD) we need brain signatures that predict the impact of multiple pathologies and their interactions. To help uncover the relationships between pathology affected brain circuits and cognitive markers we have used mouse models that represent, at least in part, the complex interactions altered in AD, while being raised in uniform environments and with known genotype alterations. In particular, we aimed to understand the relationship between vulnerable brain circuits and memory deficits measured in the Morris water maze, and we tested several predictive modeling approaches. We used *in vivo* manganese enhanced MRI traditional voxel based analyses to reveal regional differences in volume (morphometry), signal intensity (activity), and magnetic susceptibility (iron deposition, demyelination). These regions included hippocampus, olfactory areas, entorhinal cortex and cerebellum, as well as the frontal association area. The properties of these regions, extracted from each of the imaging markers, were used to predict spatial memory. We next used eigenanatomy, which reduces dimensionality to produce sets of regions that explain the variance in the data. For each imaging marker, eigenanatomy revealed networks underpinning a range of cognitive

Corresponding Author: Alexandra Badea, PhD, Center for In Vivo Microscopy, Department of Radiology, BOX 3302 Duke University Medical Center, Durham, NC 27710, USA, alexandra.badea@duke.edu.

*The first two authors share first authorship

Publisher's Disclaimer: This is a PDF file of an unedited manuscript that has been accepted for publication. As a service to our customers we are providing this early version of the manuscript. The manuscript will undergo copyediting, typesetting, and review of the resulting proof before it is published in its final citable form. Please note that during the production process errors may be discovered which could affect the content, and all legal disclaimers that apply to the journal pertain.

Author Manuscript Author Manuscript Author Manuscript Author Manuscript

functions including memory, motor function, and associative learning, allowing the detection of associations between context, location, and responses. Finally, the integration of multivariate markers in a supervised sparse canonical correlation approach outperformed single predictor models and had significant correlates to spatial memory. Among a priori selected regions, expected to play a role in memory dysfunction, the fornix also provided good predictors, raising the possibility of investigating how disease propagation within brain networks leads to cognitive deterioration. Our cross-sectional results support that modeling approaches integrating multivariate imaging markers provide sensitive predictors of AD-like behaviors. Such strategies for mapping brain circuits responsible for behaviors may help in the future predict disease progression, or response to interventions.

Keywords

Alzheimer's Disease; Behavior; Magnetic Resonance Imaging; Memory; Mouse Models; Multivariate Analysis; Predictive Modeling; Biomarkers

1. Introduction

A key question in Alzheimer's disease (AD) research is how pathology differentially and sequentially affects vulnerable brain circuits, thereby giving rise to behavioral changes. Although critically important, detailed descriptions of interactions between genes and structural and functional phenotypes are poorly described. However, these interactions dictate the vulnerability for cognitive dysfunction in the context of aging and AD related pathologies. Investigating the circuits and mechanisms underlying cognitive dysfunction is important for understanding what triggers the switch from normal aging to AD, what predicts rates of disease progression, and how patient-specific therapeutic strategies may be developed [1]. Therapies for neurodegeneration have been directed to individual targets, such as altered synaptic transmission, amyloid deposition, or abnormal tau phosphorylation - all well-demonstrated pathologies in AD [2] [3]. Additional factors, such as cardio vascular status [4] [5], insulin resistance [6], and diabetes [7] may also influence cognition [4]. Importantly, neuro-immunological mechanisms, interacting with systemic inflammatory mediators and obesity, are thought to also modulate AD pathology [5, 8, 9]. Since attacking AD pathologies separately has not yet provided effective strategies for prevention or reduction of cognitive damage, we need models that provide an integrated view of how multiple variables and risk factors contribute to system wide dysfunction. We currently lack the quantitative integrative models required to understand multifactorial conditions.

To help understand the causative links between the biological and cognitive substrates typical of AD, it is helpful to conceptualize the brain as a set of interacting regions forming a spatially distributed network [10]. Structural networks integrate effects from changes occurring at different scales (synapse, cells, circuits), which in turn modulate the properties of functional networks. Several large-scale networks have been mapped in the brain and characterized by distinct functional profiles, such as sensory perception, movement, attention and cognition [11] [12]. However, it is not well understood how brain sub-networks map to the cognitive domain. Understanding these relationships in the normal brain, and

Author Manuscript Author Manuscript Author Manuscript Author Manuscript

their alterations in disease may inform on the mechanisms underlying mild cognitive impairment (MCI) or dementias such as AD [13].

One strategy to help understand how circuits influence behavior is to link imaging to the clinical AD cognitive phenotypes. The progressive loss of cognitive memory is commonly diagnosed using tests such as the Mini–Mental State Examination (MMSE) [14], the Montreal Cognitive Assessment [15], and others [16]. Clinical populations of individuals diagnosed with AD have shown overlaps in the patterns of gray matter atrophy [17], Aß distribution [18], and axonal density changes [19], but there are also marked differences in brain atrophy [20] or tau pathology distribution [21]. Such differences may relate to population heterogeneity in terms of genetics, disease stage, or comorbidities. An alternative hypothesis to explore AD etiology is based on selective vulnerability of cells and axonal pathways favoring disease propagation. Imaging can provide *in vivo* biomarkers [22] [23] that are related to pathology as observed *ex vivo*, or to functional changes. To successfully link imaging to clinical phenotypes, we need to develop integrative models that explain the initiation, potentiation, and propagation of selective vulnerability in cells and networks that underlie AD processes, in relation to risk factors.

Neuroimaging approaches to map brain levels of behavioral descriptors have traditionally used voxel based statistical analyses (VBA) of deformation fields, structural and functional connectivity maps, vascular perfusion, or amyloid deposition and tau maps. But statistical approaches that pursue a dichotomous strategy, and aim to separate data according to image features do not necessarily explain the behavioral changes, nor do they disclose the biological processes underlying them. More recently predictive modeling approaches have been proposed to provide statistically relevant imaging correlates of memory changes spanning a continuum range, as observed in AD [24] [25] [26].

In this study, we have used a mouse model of AD to develop such predictive approaches. Mice provide tools for dissecting the contributions of genes on circuits and behavior. In particular, they provide homogenous populations, and can be tightly controlled for genetic and environmental factors, thus simplifying the problem of mapping brain circuits responsible for behavior. To establish and test a novel integrative predictive modeling approach one could choose among multiple mouse models. Most traditional models replicate one of the AD hallmarks (amyloid plaques, or tau tangles), but do not fully reflect the complex biology of AD. These transgenic mice express mutated APP [27] or PSEN1 [28], and the combination of mutations may accelerate and enhance the phenotype [29]. However, humans do not overexpress APP or PSEN1 to the same levels as in mice, and the role of beta amyloid deposition has not been fully clarified. More recently, models which also express hyperphosphorylated tau have been generated [30]. Still, most transgenic models fail to replicate other phenotypes seen in human AD, including neurodegeneration [31] [32]. Models of late onset, or sporadic AD are based on the genetic risk conferred by the presence of APOE4 alleles [33] [34] [35]. These models, while very promising in their ability to help us understand the etiology and progression of AD, require long times to express phenotypes, including behavioral deficits. None of these models addresses the differences between the mouse and the human innate immune systems, and the potentially important role of microglia in the development of AD [36]. For example the nitric oxide levels produced by

Author Manuscript Author Manuscript Author Manuscript Author Manuscript

immune activation of the NOS2 gene mouse are much higher than in humans [37]. In the ***APPSwDI***$^{+/+}$/*mNos2*$^{-/-}$ (CVN-AD) strain [38, 39], *mNos2* deletion makes the immune responses more similar. In conjunction with the Swedish, Dutch and Iowa mutations, this promotes an AD-like background required for studying the underlying mechanisms of pathological regional vulnerability. CVN-AD mice replicate multiple AD pathologies, including amyloid and tau deposition, neuronal loss, altered microglial activity with typical AD-like inflammatory patterns and deficits in memory and learning [38, 40] [41] [37] [42] [43]. The appearance of cognitive deficits with aging in this strain mimics processes in humans with AD and can be assessed using the Morris water maze test. This behavioral test is commonly used to quantify the loss of spatial learning and memory in animal models of aging and AD [44, 45].

To map behavioral changes to specific brain regions and networks we have used *in vivo* manganese enhanced MRI (MEMRI). Manganese ions (Mn^{2+}) are paramagnetic and induce T1 shortening [46], enhancing tissue contrast [47]. Mn^{2+} has also been used to characterize trans-synaptic connectivity and axonal transport properties in rodents [48, 49] [50]. Importantly, Mn^{2+} enters neural cells via voltage gated calcium channels and vesicular reuptake, presenting an alternative for task based fMRI in rodents [51] [52], while alleviating limitations due to the types of tasks that animals can perform in the magnet, or to anesthesia [53]. These strategies to characterize brain structure and function in CVN-AD mice in relation to age matched controls can identify vulnerable brain circuits responsible for behaviors typical of AD.

To identify vulnerable regions and networks that predict deficits in memory and learning, we used an integrative approach that was not linked to a single identified neuropathological mechanism, but was reflective of multiple concomitant factors. We evaluated how traditional mass-univariate analyses can predict behavior dysfunction, and followed with a multivariate approach involving dimensionality reduction. Eigenanatomy, a sparse dimensionality reduction method, was incorporated to extract brain regions responsible for changes in morphometry, signal intensity due to Mn^{2+} uptake (reflective of brain activity), and magnetic susceptibility (reflective of altered iron homeostasis and conducive to oxidative stress and inflammation) [54] [55]. However, these methods analyzed individual biomarkers separately. We have employed both a data-driven as well as a hypothesis-driven approach to associate imaging phenotypes with behavioral markers for cognitive status and to identify circuits vulnerable to AD like pathology. Eigenanatomy produced candidate regions and circuits, and we selected regions that appeared important based on one or more biomarkers, and confirmed by previous studies as relevant to AD. To predict cognitive dysfunction based on *in vivo* multivariate imaging markers we used sparse canonical correlation analysis (SCCA) [56, 57]. SCCA selects regions so to maximize correlation among imaging and cognitive measures, in a supervised approach. The result is a network of regions that underlie changes in cognition, incorporated in a multivariate analysis. Our results provide insight into the relationships between structural networks and cognitive function in animal models of AD, supporting the value of multivariate approaches for humans with AD.

Author Manuscript Author Manuscript Author Manuscript Author Manuscript

2. Materials and Methods

To test the hypothesis that we can identify vulnerable brain circuits involved in behaviors where aged mouse models for Alzheimer's disease (AD) differ relative to their age matched controls, we used *in vivo* multivariate magnetic resonance imaging (MRI) and the Morris water maze test for spatial memory. Our strategy examined each biomarker at a time, as well as an integrative predictive modeling framework.

2.1 Animals

The study was conducted under protocols approved by the Duke IACUC. CVN-AD (*APP*SwDI/*mNos2*$^{-/-}$) (11 mice) and *mNos2*$^{-/-}$ controls (13 mice), aged 75. 9 ± 4.4 weeks were handled and acclimated to water for 5 days. To contrast AD like phenotypes in CVN-AD mice we compared them to *mNos2*$^{-/-}$ mice, which we found to perform similarly to WT mice [42], and WT mice were not included in the present experiment. Mice were then implanted with Alzet 1007D minipumps (Durect Corp, Cupertino, CA), containing 100 μl of 64 μm/μl $MnCl_2$*4(H_2O) (Sigma Aldrich, St Louis, MO), in 100 mmol bicine (Sigma-Aldrich, St Louis, MO). Animals were acclimated for 3 days following pump implantation, before behavioral testing. A summary of the experimental design is shown in Fig. 1.

2.2 Behavioral Testing

To test spatial memory which declines in AD, we used the hidden platform Morris water maze. For 5 days, mice received 4 trials a day (of maximum 60 s each), in trial pairs (60 s between trials) separated by 60 min intervals. Probe trials were run 60 minutes after the last trial on days 3 and 5. Swim time and distance were measured using Ethovision (Noldus Information Technology, Blacksburg, VA). Statistical analysis used SPSS (IBM, Armonk, NY), and included a repeated measure ANOVA, followed by Bonferroni corrected posthoc tests. A p-value < 0.05 was considered significant.

2.3 Imaging

In vivo imaging was done using a 7 T, 20-cm bore Bruker BioSpec 70/20 USR magnet (Bruker Biospin, Billerica, MA), interfaced to an Avance III console. The scanner has actively shielded gradients with integrated shims. The 198/114 mm outer/inner diameter insert gradient coil can supply 440 mT/m, at a slew rate of 3440 T/m/s, and rise time of 110 μs. We used a quadrature radio frequency transmit-receive cryogenic coil.

Two protocols were used to image the mouse brain at 100 μm resolution. To quantify morphometric changes and manganese uptake we used a T1-weighted (T1w) Rapid Imaging with Refocused Echoes (RARE) sequence with field of view (FOV) 2×2×1 cm, matrix 200×200×100, number of excitations (NEX) =2, BW =100 kHz, min echo time (TE) =10.3 ms, effective echo time TEeff=20.6 ms, repetition time TR =150 ms, echo spacing 10.3 ms, RARE partitions 4, acquired in 23 min. To estimate quantitative susceptibility maps we used a multi echo gradient recalled echo (mGRE) with field of view (FOV) 1.92×1.92×0.9; matrix 192×192×90, 8 echoes with spacing of 5.5 ms, number of excitation (NEX) =1, 1st echo time (TE1) =3.9 ms; repetition time (TR) =100 ms, flip =30°, bandwidth (BW)=62.5 kHz, respiratory gated, acquired in ~30–40 mins.

Author Manuscript Author Manuscript Author Manuscript Author Manuscript

To ensure reproducible positioning, mice were restrained in a cradle equipped with ear bars, and a nose cone for isoflurane delivery (1.5±1%). Animals were monitored throughout the experiment, temperature and respiratory rate being maintained at physiological levels (37°C, 70–110/min) by circulating warm water under the cradle, and adjusting the anesthesia level.

2.4 Image Preprocessing

Images were bias field corrected [58], skull stripped [59], and the resulting brain masks were manually edited. All brain images were rigidly aligned into the Waxholm space [60], and averaged to create a minimum deformation template [61] [62]. The template was labeled with a set of 332 regions, symmetric for the left and right hemispheres [63], defined on a single mouse brain [64]. To estimate morphometric differences, we used the log-transformed Jacobian determinants of the deformation fields (logJAC), mapping individual brains to the average. This enables comparisons with a symmetric distribution, with the same prior probability for shrinkage or expansion [65]. We used the T1-weighted images, where the voxel intensity reflects Mn^{2+} uptake, which happens at least partly through calcium channels, to provide estimates of neuronal activity independently of hemodynamic activity [66]. Average T1-weighted manganese enhanced MRI (T1wMEMRI) voxel values for each mouse brain were normalized to a reference brain value. We calculated quantitative susceptibility maps (QSM) sensitive to iron, amyloid accumulation, and myelin using STI Suite [67]. Susceptibility values were directly used for comparison without referencing to any selected region of interest, which essentially sets the susceptibility reference to the mean susceptibility of the whole structure within the FOV. STI Suite uses a Laplacian-based method to unwrap the phase, after which the background is eliminated using vSHARP [68]. The corrected phase images were combined, weighting the two channels. We used a two-step streaking artifact reduction regularized reconstruction (STAR-QSM) [69], which optimally weighs data consistency and smoothness for both high and low susceptibility variations.

2.5 Voxel Based Analysis

All three contrast images (log Jacobian, normalized T1-weighted RARE, and QSM) were mapped into the space of the minimum deformation template, and smoothed with a 200 μm kernel. This kernel was selected to highlight the scale of features at which we expect to detect pathology-related differences across these MRI-based measurements. The Statistical Parametric Mapping SPM toolbox, version 12 [70] was used with voxel-wise false discovery rate correction.

2.6 Eigenanatomy

We hypothesized that eigenanatomy [25], a sparse dimensionality reduction technique, will confer increased power to detect differences between genotypes. The method approximates an eigen decomposition of an image set with spatial basis functions (eigenanatomy vectors) that are unsigned, sparse, and anatomically clustered. We employed the eigenanatomy vectors as anatomical and functional imaging predictors. We leveraged the technique in two stages: first, to reduce the dimensionality in an unsupervised setting; second, to perform a supervised regression within the setting of cross-validation.

Author Manuscript Author Manuscript Author Manuscript Author Manuscript

The goal of eigenanatomy is to identify sparse functions which approximate the eigenvectors ($v^p = X^T v^n$ *and* $v^n = X v^p$) of the $n \times p$ image matrix X, where each row n represents the data for one subject, and has p entries (voxel values). The method approximates X with i sparse singular vectors v_i^{sp}, treating the positive (v_i^{sp+}) and negative components (v_i^{sp-}) separately, and imposes positivity constraints on both:

$$\underset{v_i^{sp+},\, v_i^{sp-}}{argmin} \left\| X^T X v_i^{sp+} - v_i^{p+} \right\|^2 + \left\| X^T X v_i^{sp-} - v_i^{p-} \right\|^2;\ \text{subj.}\ \text{to} \left\| v_i^{sp+} \right\|_1 = \left\| v_i^{sp-} \right\|_1 = \gamma \quad \text{(Eq.1)}$$

where γ is the sparseness parameter. The weight on the L1 penalty is set to reach the desired sparseness and guarantees that only a subset of voxels is considered [56] [71]. The minimization uses a nonlinear conjugate gradient, with sparseness imposed through soft thresholding S(v, γ), which rejects clusters below a threshold. The resulting pseudo-eigenvectors are sparse, unsigned, and represent the input data (X) through weighted averages.

To estimate the generalization performance for our models we divided the data in training and testing groups (75%, and 25%), and we used a 4-fold cross-validation, as described in [72]. We assigned data to training (n=18), and validation (n=6) partitions in a balanced way using caret (caret.r-forge.r-project.org/), then evaluated the average root mean square error (RMSE) over the test partitions. Dimensionality reduction was performed using the function *sparseDecom* in ANTsR (https://github.com/ANTsX/ANTsR) for each of the imaging contrasts (logJac, T1wMEMRI, QSM), producing areas that have maximum covariance between subjects. For each imaging contrast we used 2 eigenvectors, a sparsity threshold of 5%, and a min cluster size of 250 voxels, or 6 eigenvectors for all three imaging contrasts used in the multivariate approach. These parameters were chosen to balance interpretability and anatomical specificity. The choice of two vectors/contrast enable analogous comparisons between the VBA analyses (pos+neg clusters) and our sparse decomposition based approaches. Clustered signal smaller than 250 voxels (roughly 0.25 mm^3) are difficult to interpret. Furthermore, extended components (> 5% of the brain) are less specific and tend to converge towards the mean signal over the whole brain.

These eigenregions were projected against the training set to generate statistical models that predict swim distance at day 4. The summary of the statistical models performance applied to the testing sets included the RMSE, Pearson correlation, adjusted R^2 and p value (considered significant at $p<0.05$).

2.7 Prior-Based Prediction Using Sparse Canonical Correlation (SCCAN)

We used an anatomically informed, prior-based approach to constrain the solution space, to test whether specific brain regions were associated with cognitive performance. These regions were determined based on: 1) eigenanatomy results, producing a supervised decomposition, and 2) anatomical priors on regions known for their involvement in AD, and which are recognizable in mouse models. These regions included the hippocampus,

Author Manuscript Author Manuscript Author Manuscript Author Manuscript

parasubiculum, and fornix [73] [74] [75, 76], as well as the entorhinal and motor cortices. Each of these regions is likely to incur changes during training in the water maze. These regions were used to initialize SCCAN [71] to infer their influence on behavior.

We hypothesized that we could identify brain networks associated with behaviors based on canonical correlation (CCA) [77], the multivariate extension of correlation analysis. To find the linear projections of two random vectors, CCA maximizes the correlation between the two linear combinations of the variables in each data set. Our datasets consist of imaging (X) and behavioral parameters (Y) for n subjects. The imaging parameter is a large $n \times p$ multidimensional matrix, and the behavioral parameter is $n \times q$, where p is the number of voxels in X for each subject, and q is the number of behavioral parameters in Y for each subject.

Due to the greater size of the imaging matrix compared to behavior, CCA becomes ineffective. Instead sparse CCA has been used as a dimensionality reduction method to produce the solution vectors, $x\,(p \times 1)$ and $y\,(q \times 1)$, which act as weights on columns of X and Y [71].

$$x^*, y^* = \underset{x,\,y}{argmax} \frac{(Xx)^T Yy}{\|Xx\|\|Yy\|};\ subject\ to \sum_j \left\|x^j\right\|_1 \le s, x^j \ge 0 \qquad \text{(Eq.2)}$$

The x^* solution vector is subjected to the "L_1" norm, $\|.\|_1$, producing non-zero entries below the chosen sparsity threshold [26]. The gradient of the objective function in (Eq.2) is calculated with respect to x and y. A nonlinear gradient descent optimizer is used to provide the solution vectors. Additionally, a cluster threshold and a smoothness constraint are enforced to retain anatomically meaningful brain regions. As a result, sparse CCA produces solution vectors x^* and y^*, dimensioned as subsets of variables that maximize the correlation between imaging and behavior.

Here we focused on a single vector to represent behavioral performance, i.e. swim distance at day 4 (SD4). We used sparse canonical correlation (SCCAN) to perform a sparse regression between imaging and behavior.

$$\underset{x}{argmin} \frac{1}{2}\left\|Xx - y\right\|_2^2 + \frac{\lambda_1}{2}\left\|x\right\|_2^2 + \frac{\lambda_2}{2}\left\|\nabla x\right\|_2^2;\ subject\ to \left\|x\right\|_1 \le S \qquad \text{(Eq.3)}$$

where s is the desired sparseness, λ_1 a ridge penalty which alleviates the problem of multicollinearity amongst regression predictor variables, and λ_2 a smoothness penalty, and ∇ denotes the gradient operator. This is solved through a projected gradient descent [26]. We note that in recent approaches the L0 penalty, which guarantees that only a subset of voxels is considered for the model, has been replaced with the convex approximation given by an L1 penalty, which yields virtually identical results, in a robust approach to regression [78] [26]. The soft thresholding operator was used to update the sparse projection of the solution vectors at each step of the optimization.

Author Manuscript Author Manuscript Author Manuscript Author Manuscript

We used SCCAN for a positively constrained optimization that finds projection vectors in the minimum deformation template space, which maximizes the relationship between image markers (for each of the three separate contrasts, and in combination) and swim distance at day 4. The inputs for SCCAN included the training set for both imaging and swim distance (SD4) through the function *sparseDecom2* [79].

Both the imaging and behavioral data were split into training and testing sets in a ratio of 75:25, which allowed for 18 variables/subjects for training and 6 for testing. We chose the SD4 as the behavior to be predicted based on its robust ability to separate the groups. The sparse canonical correlation was initialized from each of the *a priori* selected image regions (1 eigenvector), using a medium prior (0.5). We used sparseDecom2 with 5% sparseness, 250 voxels cluster threshold, 15 iterations. No sparsity constraints were enforced on behavior. The projection vectors obtained from the training set model the relationship with behavior. These models were then used to predict swim distance for the testing set. To assess the quality of the predictive modelling approach we determined the relationship between the predicted and measured SD4.

We examined how the solution vectors from sparse CCA of different imaging contrasts performed as predictors on unseen behavioral data. We aimed to identify brain regions with a reliable association between each imaging marker and behavior using sparseDecom2, with a sparseness value that selects a small, informative subset of voxels (250 voxels, and 5% sparsity). Finally, the resulting eigenregions were used to fit a linear model to SD4. Our modeling approach is summarized in Fig 2, for one single imaging contrast at a time. The combined biomarkers modeling uses image concatenation in an easy extension of this approach.

We tested several models to predict behavior based on imaging biomarkers using a 4-fold cross validation scheme. First, we examined how the clusters surviving false discovery correction (FDR) in the VBA in the three different imaging contrasts performed as predictors for behavioral data. We compared the performance of these models with those generated from the sparse decomposition (SD) for each of the imaging contrasts. Finally, we fused the information from all imaging contrasts in a behavior supervised sparse decomposition (SSD) that maximized the canonical correlation between imaging and swim distance. This approach was used in a hypothesis generating mode throughout the whole brain to identify brain circuits responsible for AD like cognitive decline, as well as to test our hypotheses for regions expected to be involved in memory or motor function.

All prediction methods were executed using R (www.r-project.org) and the ANTsR package (http://stnava.github.io/ANTsR/). The compute times required for each fold in our optimization experiments ranged from 2 minutes (for 2 vectors, 5% sparsity) up to 2 hours and 22 minutes (for 50 eigenvectors, 5% sparsity), using a MacPro equipped with 12 cores, 2.7 GHz Xeon E3 processors, running 10.13.6 Mac OS Sierra.

FSLEyes (https://fsl.fmrib.ox.ac.uk/fsl/fslwiki/FSLeyes) was used for visualization of statistical parametric maps overlaid on the average T1-weighted manganese enhanced MRI (T1wMEMRI) template generated from *mNos2*$^{-/-}$ controls.

Author Manuscript Author Manuscript Author Manuscript Author Manuscript

We used a sodium borohydride method to stain for iron deposits. We used a modified Gallyas silver staining method for white matter [80]. We used the Abeta 700254 antibody from Invitrogen, the NeuN MAB377 antibody from Chemicon for neurons, GFAP 13–0300 antibody from Zymed for reactive astrocytes, and the CD11c MCA1369 antibody from AbDSerotec for activated microglia.

3. Results

To help uncover the relationship between cognition and the biological substrates underlying AD, experiments were carried out using a well-characterized mouse model of AD, to reduce genetic and environmental diversity. Behavior and imaging data were subjected to univariate and multivariate analyses.

Spatial memory was examined through acquisition and probe trial performance in the Morris water maze (Fig. 3). Swim distance and swim time to the hidden platform declined across testing for both genotypes (Fig. 3A–B). Significant genotype effects emerged on block trials 3–5, where swim distances decreased in the *mNos2*$^{-/-}$ control mice relative to the CVN-AD strain ($p \leq 0.050$) (Fig. 3A). Within genotype, swim distances decreased from trial 1 to trials 3–5 in *mNos2*$^{-/-}$ control mice ($p \leq 0.002$), whereas in CVN-AD animals this parameter only declined from trial 1 to 5 ($p=0.005$). A similar relationship was observed for swim time (Fig. 3B). Here, swim times were reduced significantly on trials 3 and 4 for the *mNos2*$^{-/-}$ compared to CVN-AD animals ($p \leq 0.025$). Within genotype, swim times in *mNos2*$^{-/-}$ animals declined from trial 1 to trials 3–5 ($p<0.001$). By comparison, in CVN-AD mice swim time was decreased only from trial 1 to 5 ($p=0.001$).

Analysis of learning performance on the probe trials for swim distance and swim time further demonstrated that the CVN-AD mice were deficient in this task (Fig. 3C–D). On day 3 *mNos2*$^{-/-}$ control mice swam over longer distances in the target northeast (NE) quadrant, whereas CVNAD mice had not made this distinction (Fig. 3C). Thus, on day 3 CVN-AD animals swam over shorter distances in the NE target ($p=0.026$) and longer in the northwest (NW) and southwest quadrants than *mNos2*$^{-/-}$ controls ($p \leq 0.018$) (Fig. 3C, *left*). On probe day 5, *mNos2*$^{-/-}$ animals maintained increased swim distances in the target quadrant, whereas in CVN-AD mice swim distances were longer in the NE and northwest than the other quadrants (Fig. 3C, *right*). On this probe trial, the only genotype difference was in the northwest quadrant where CVN-AD mice swam over a longer distance than *mNos2*$^{-/-}$ controls ($p=0.003$). Similar relationships were observed with swim time (Fig. 3D). With the probe trial on day 3, *mNos2*$^{-/-}$ mice swam for longer times in the NE target quadrant ($p=0.002$) and shorter times in the northwest ($p=0.004$) with a trend for the southwest ($p=0.064$) quadrant compared to the CVN-AD animals (Fig. 3D, *left*). By day 5 probe trial, swim time remained augmented in the northwest quadrant for the CVN-AD mice ($p=0.045$) (Fig. 3D, *right*). These results indicate that the CVN-AD mice had learned that the north quadrants contained the target, but they were unable to discriminate the NE from the NW quadrant. Collectively, these results demonstrate that acquisition duration in the Morris water maze is prolonged in CVN-AD mice, which fail to identify the NE quadrant as the target zone in the probe trials.

Author Manuscript Author Manuscript Author Manuscript Author Manuscript

We have also examined the three-way interaction between genotype, probe day and zone, and compared the zone activity within genotype and for each of the two probe days (Fig. 3). Bonferroni corrected *a posteriori* tests showed that *m*NOS2$^{-/-}$ mice traveled more in the target NE quadrant compared to the SE ($p<0.002$) quadrant, and showed a trend relative to the NW ($p=0.069$) and SW ($p=0.077$) quadrant. This difference was also observed in the controls on day 5, with a significant difference between the NE and NW quadrant ($p<0.039$) and marginal differences between the NE and the SE ($p=0.079$), but non-significant relative to the SW ($p=0.262$) quadrant. Hence, the distance moved in the four quadrants and marked preference for the NE quadrant was stable on day 5 compared to day 3 in the mNOS2$^{-/-}$ mice. By comparison, the CVN-AD animals failed to show significant preferences for the NE target quadrant on the day 3 probe test compared to the other quadrants and did travel more in the NW or SW quadrants, although these differences were not statistically significant. On day 5 probe testing the CVN-AD mice increased the distance in the NE quadrant compared to that measured on day 3 ($p<0.058$), however, this still did not produce a significant difference between the NE and the remaining quadrants. Hence, compared to the *m*NOS2$^{-/-}$ mice, the CVN-AD animals showed reduced preference for the NE quadrant on day 3 ($p<0.026$), and increased preferences for the NW ($p<0.003$) and SW ($p<0.018$) quadrants compared to the mNOS2$^{-/-}$ animals. By probe day 5, the increase observed in the NE quadrant by the CVN-AD mice made that activity equivalent to that observed in the *m*NOS2$^{-/-}$ animals for that quadrant on the same day. Although the CVN-AD mice continued to travel more in the adjacent NW quadrant ($p<0.003$) compared to the mNOS2$^{-/-}$ mice on day 5, no differences were detected between these two groups for the SE and SW quadrants. For the probe swim time, Bonferroni corrected post-hoc tests found significant overall genotype differences within the NE target quadrant ($p<0.008$), and the adjacent NW quadrant ($p<0.002$); however, no differences were found between the two southern quadrants. Overall, while the *m*NOS2$^{-/-}$ mice spent more time swimming in the NE zone compared to the NW ($p<0.001$), SE ($p<0.001$) and SW ($p<0.004$) quadrants, the CNV-AD mice failed to exhibit significant differences between the NE and remaining zones. Although the within subjects contrast three-way interaction approached significance, it's important to note that the Bonferroni post-hoc comparisons did show that the genotypes had significant differences on the first probe test within the NE quadrant ($p<0,002$) with the CVN-AD mice spending less time in the target zone. However, by the final probe test, no differences in the swim time existed between the two genotypes ($p=0.305$). These results show that on test day 3 the CVN-AD mice are delayed in discriminating the target NE quadrant in the water maze, but by day 5, there is a marginal preference for the target quadrant, although this is not absolute as found in the *m*NOS2$^{-/-}$ animals.

Since in the acquisition test genotype differences were most robust on trial 4 for swim distance, and provided a clear separation of the two genotypes, these data were used as the dependent variables for predictive modeling.

We have implemented two manganese enhanced MRI (MEMRI) protocols to characterize anatomy and memory function based on: 1) the log-jacobian of the deformation fields; 2) the T1-weighted signal intensity (normalized to the average value determined for a reference brain); and 3) quantitative susceptibility maps (QSM). Representative images for one animal are shown in Fig. 4A. We constructed minimum deformation templates (MDT) as study

Author Manuscript Author Manuscript Author Manuscript Author Manuscript

specific population atlases for each of these contrasts (Fig. 4B), and derived Jacobian and QSM maps (Fig. 4C).

We sought brain networks for which changes in imaging markers explain changes in behavior. Using regional and voxel based analyses (VBA) we identified significant changes in volume (Jacobian of deformation fields), manganese accumulation (normalized T1-weighted signal intensity), and quantitative susceptibility maps (QSM). All image contrasts identified differences in the olfactory areas, hippocampus, entorhinal cortex, and cerebellum, and the volume and T1wMEMRI analyses revealed a role for the retrosplenial cortex (Fig. 5).

The reductions in volume in olfactory areas, thalamus, and hippocampus were accompanied by increased magnetic susceptibility, and lower manganese uptake (Fig. 5 A–D). Areas of the entorhinal cortex, hippocampus and subiculum showed decreased susceptibility. Increases in susceptibility were noted in the caudate putamen and red nucleus. T1wMEMRI signal intensity was overall lower on CVN-AD mice, and local differences between genotypes were significant at FDR 0.2 in the olfactory areas, motor cortex, primary somatosensory (S1) cortex, hypothalamus, and hippocampus, in particular the dentate gyrus and subiculum, and cerebellum. A more extensive presentation of the regional results can be found in the Supplementary Tables.

Separate analyses for volume, T1wMEMRI signal and QSM were conducted using the clusters with significant VBA differences between the two groups to model the relationship with behavior (Fig. 5E). Among the individual contrasts volume was ranked as the best predictor, followed by T1wMEMRI signal, then QSM. The root mean square error (RMSE) ranged from 259±57 cm for clusters with significant atrophy, to 274±54 cm for clusters with decreased T1w signal, while the largest RMSE was obtained for the combined QSM clusters (290 ±51cm). Table 1 reports the performance of all tested methods to produce the final models based on the 4-fold cross validation (testing) RMSE, the correlation and variance explained by each method, and their rank in terms of predictive performance.

We then used eigenanatomy to identify areas of the brain with maximum covariance between subjects, producing a sparse decomposition (SD) for each of the imaging contrasts. The eigen regions based on volume revealed a network comprised of the frontal pole, septum, medial thalamus, retrosplenial and cingulate cortex, amygdala, the CA1 area of hippocampus, and fimbria. In addition, we noted the involvement of sensory and motor cortices, and of the caudate putamen (Fig. 6A, **top row**).

The T1wMEMRI signal intensity-based decomposition revealed a network including olfactory areas, the cingulate cortex, bed nucleus of stria terminalis, substantia innominata, amygdala and hippocampus (Fig. 6B, **top row**).

The QSM based decomposition revealed involvement of the olfactory areas, septum, and cingulate cortex, the hippocampus, bed nucleus of stria terminalis, substantia innominata. Iron rich regions were also involved such as the substantia nigra, caudate putamen and globus pallidus (Fig. 6C, **top row**).

Author Manuscript Author Manuscript Author Manuscript Author Manuscript

By adding elements of supervision through the sparse canonical correlation of imaging and behavior we observed additional areas relative to the networks identified before. These included the fornix, dorsal thalamic nuclei, as well as the ventricles for the volume based decomposition (Fig. 6A, **bottom row**); the medial thalamic nuclei for the T1wMEMRI based decomposition (Fig. 6B, **bottom row**); white matter such as the anterior commissure and corpus callosum (including areas below the motor cortex and S1) for the QSM based decomposition, and more extensive areas on the ventral hippocampus and primary somatosensory cortex (Fig. 6C, **bottom row**).

Specific brain areas (eigen regions) found to be common in the results for all three contrasts (Fig. 6D). included the olfactory, cingulate cortex and retrosplenial cortex, hippocampus, as well as the motor cortices, and septum. The substantia innominata and bed nucleus of stria terminalis were common to T1wMEMRI, and QSM.

Using a supervised approach and the combined regions from volume, T1wMEMRI and QSM provided the lowest RMSE of 233.08 ±101.78 cm, a significant correlation of 0.94, explaining 88% of the variance in the swim distance. The tightest confidence intervals and largest adjusted R2 were obtained using the multivariate supervised approach (Fig. 6E, and Table 1).

A nonparametric Kruskal Wallis test did not reveal a significant difference for the generalization performance estimated based on the 4 fold cross-validation (testing RMSE) for all models ($p=0.09$, chi square=22.9, df=15). To evaluate the 16 models' performance, we compared their predictions with the measured values for the swim distances for the full data set. The Kruskall–Wallis analyses were followed by posthoc Tukey Kramer tests to control for the family wise error rate. Our results (Table 2, Fig. 7) indicated that the supervised multivariate approach outperformed 12 of the other models ($p=6.9*10^{-5}$, chi=45.3, df=15). These analyses also indicated that amongst the individual imaging contrasts studied, volume was the best predictor for behavioral performance in the water maze, followed by QSM, and then T1wMEMRI.

To test whether structures about which we have previous hypotheses are predictive of behavioral performance in the Morris water maze, we selected regions that appeared significant in one or more of the single biomarker analyses. These regions play a role in spatial memory and included the hippocampal formation, entorhinal cortex, parasubiculum, fornix, the primary and secondary motor cortex. Fig. 8 shows the predictive correlation for these models. The RMSE and significance of the models predicting relationships between imaging and behavior generally improved or were similar to the best predictor when the model included all three factors (Table 3). However, the single region analysis underperformed relative to the whole brain supervised sparse decomposition (SSD) analysis, with a maximum correlation of 0.76 for the parasubiculum in the combined analysis (explaining 56% of the variance), and 0.73 for its volume (explaining 51% of the variance). This suggests that our animals model a complex, network- rather than a region-based disease.

Author Manuscript Author Manuscript Author Manuscript Author Manuscript

4. Discussion

Neurodegenerative conditions such as AD arise from multifactorial pathological processes. Integrative modeling is an important step towards better understanding this complex disease etiology, as well as predicting its trajectory. Recent efforts to produce models for disease progression and response to treatment have shown promise in AD patients, and cognitively normal people at risk for AD [81]. However, the genetic variability and differences in environmental conditions to which patients have been exposed make these studies difficult. Animal models provide attractive tools for conceptually advancing our understanding of complex pathological processes, and factor to factor interactions. Moreover, animal models are required for testing therapeutic interventions. Hence we used a mouse model [40], previously characterized using pathology [41], and *ex vivo* diffusion tensor MRI [76], and whose development of cognitive dysfunction mimics the development of AD [41].

Our results support previous findings on learning and memory deficits in mouse models of AD [82], [83, 84]. Such deficits have been associated with the presence of amyloid [84, 85], tau [86], altered synaptic plasticity [87], or to inflammation and neurodegeneration [82] [41] [42]. The impairment in the acquisition of the Morris water maze was evident for CVN-AD mice relative to $mNos2^{-/-}$ controls when both swim distance and swim time were analyzed. These deficiencies were verified in the probe trials where CVN-AD mice failed to discriminate the target quadrant from the other quadrants early in testing and from the northwest quadrant at the end of testing. Our results thus confirmed that CVN-AD mice were impaired in spatial memory, in agreement to previous publications [41] [43]. Moreover, we identified swim distance during the 4^{th} day of trial test as a robust measure that allows clear differentiation of CVN-AD models from age matched $mNos2^{-/-}$ controls.

To bridge between structural and functional imaging correlates, we used manganese, which modifies MRI signals and accumulates during behavioral training and testing. Manganese increases image contrast due to differential uptake by various brain areas [88], [89, 90]. We have used this property to more accurately estimate morphometric changes *in vivo*. T1 shortening occurs as a consequence to intracellular manganese uptake, upon neuronal excitation/depolarization. Our use of MEMRI is equivalent to a spatial memory -based fMRI, with the limitation that it lacks the temporal resolution, and we showed that MEMRI can be used to map complex brain circuits involved in spatial memory.

The observed decrease in MEMRI signal after behavioral testing supports the loss of neuronal activity in memory circuits in old CVN-AD mice. A loss of MEMRI signal has also been demonstrated in mouse models of tauopathy [52, 91]. In contrast, MEMRI signal was shown to increase 24 h after MnCl2 injection in young 5xFAD mice [92]. This model of AD demonstrates abundant amyloid deposition generated from a high level of overexpression of mutated human amyloid precursor protein [93]. In addition to the differences between mouse models, the differences between these studies results may be explained by two effects: 1) high neuronal activity was present in younger mouse models of AD, and later decreased with age, and/or 2) our study measured a functional effect related to maze training, specific to memory function and diminished in older models of AD.

Author Manuscript Author Manuscript Author Manuscript Author Manuscript

The T1 weighted MEMRI (T1wMEMRI) images suggested decreased Mn movement into the cells in CVN-AD models, in particular in olfactory areas, the hippocampus, hypothalamus, motor cortex, and also the cerebellum. The lower manganese uptake in CVN-AD mice was accompanied by atrophy in the olfactory areas, thalamus, and hippocampus, and was also associated with increased magnetic susceptibility. However, a reduced brain activity was expected to cause susceptibility reduction. Indeed, several areas of the hippocampus, entorhinal cortex and parasubiculum had lower susceptibility values in AD models. A decrease in susceptibility can be attributed to reduced manganese uptake, and also to diamagnetic properties of amyloid, or myelin. QSM increases did however overlap with areas of volume reduction, possibly associated with cellular and dendritic density reduction, leading to loss of anisotropy. QSM increases were noted in the hippocampus, olfactory areas, and red nucleus. VBA also identified QSM increased in iron rich areas, such as the globus pallidus and caudate putamen. Alterations in iron metabolism or the presence of microbleeds may lead to the observed predominant susceptibility increases. The increased susceptibility in areas such as the caudate putamen [94] and hippocampus was associated with decreased T1wMEMRI values, thus could result from the higher level of iron from neurofibrillary tangles, and the aggregation of iron containing amyloid plaques. Hippocampal QSM increase has been associated with amyloid pathology in humans, moreover it was predictive of faster cognitive deterioration [95].

A qualitative evaluation of histopathological features from age matched CVN-AD and age matched control animals (Fig. 9) illustrated several factors which could have affected imaging biomarkers, and in particular QSM values in CVN-AD mice. The histological markers included amyloid beta, iron staining (ferritin), myelin, as well as inflammatory changes. Amyloid beta deposition would lead to decrease in QSM in the hippocampus, and was also seen in the subiculum, and entorhinal cortex. However, our VBA results also identified QSM changes due to iron presence, in the hippocampus and in areas known to be rich in iron, such as the globus pallidus. These resulted in increased QSM in CVN-AD models. Reduction in myelination would lead to increased QSM, but the resolution of in vivo scan may not be sufficient to resolve such changes in small white matter tracts, however we observed such effects previously as well [76]. QSM changes do however overlap with areas of volume reduction, possibly associated with cellular density reduction (NeuN), leading to loss of anisotropy. Activated astrocytes and microglia may also result in microstructural changes, and possible damage to myelin.

VBA revealed that morphometric changes survived the highest stringency in thresholded statistical maps, relative to QSM and T1wMEMRI signal reflecting manganese uptake. Significant changes in all three parameters were present in olfactory areas, septum, hippocampus in specific layers and the dentate gyrus, subiculum, and cerebellum.

Since mice perform a complex task during Morris water maze testing, which also involves swimming, it is not surprising to find that key regions realizing intentional motor control (including the cingulate cortex) are involved [96]. Not only does this region have a role in consolidating object/place association memories [97], but is has extensive connections to other brain areas. In primates, the cingulate cortex has been shown to have structural

Author Manuscript Author Manuscript Author Manuscript Author Manuscript

connections with limbic regions/temporal cortex, but also to supplementary motor areas, premotor as well as parts of the prefrontal cortex, and insula.

In summary, while the exact pathology underlying the observed changes remains unclear, these may be attributed to atrophy associated with neurodegeneration (or conversely, increases due to astrogliosis), to reduced manganese uptake and myelin loss; or to amyloid and abnormal iron deposition.

As shown previously for other amyloid based mouse models, we found enlarged volumes in some areas of the brain, particularly the somatosensory cortex, cerebellum, and the corpus callosum. Such changes have been observed in multiple mouse models of AD including the TgCRND8 [98], APPJ20 [99], PSAPP, and Arc [100], and are generally in contrast to the pathology commonly observed in AD patients. AD is associated with cortical thinning and cortical volume loss [101]. However, heterogeneity has been demonstrated in human studies. Increased volumes have been observed in APOE4 positive AD patients [102], particularly in early stages. Whole brain, cortical, and hippocampal volume increases due to APP or PS1 transgenes have been also reported in humans and have been attributed to amyloid deposition [103], gliosis [104], increased extracellular space, cellular swelling in response to toxicity, or to a compensatory mechanism [105].

Among phenotypic differences assessed with VBA, volume ranked best for its ability to predict memory. We used eigenanatomy [25] to exploit the covariance in a dataset, and identify a reduced set of voxels, assembled into coherent regions. We then used regression in this reduced dimensionality space to identify associations with spatial memory. The regularized sparse decomposition (SD) identified that the volume of the cingulate and motor cortex areas had good predictive value for spatial memory. Additionally, the decomposition solutions based on T1wMEMRI signal revealed that lower activity in the limbic thalamus, in the motor, cingulate and entorhinal cortices, as well as in the globus pallidus, were all predictive of the behavioral performance. Some of these areas were also present in the decomposition solutions based on susceptibility, which emphasized the role of the olfactory, motor, cingulate, and hippocampal areas.

While distinct regions were associated with behavior for different imaging parameters, a number of these regions were common between the three contrasts, and were overlapping with areas known to be involved in AD. These involved a network including septum, hippocampus, cingulate, retrosplenial and motor cortices. Our results also suggest a role for limbic thalamic nuclei, substantia innominata and amygdala. While the eigenregions were more extensive than the clusters obtained from VBA, these were also likely to be involved in multiple behaviors, such in motor planning and execution of the task, besides spatial memory.

Motivated by such hypotheses we have integrated multivariate imaging biomarkers into a modeling framework to map brain circuits that predict performance in the water maze. We selected regions identified as important in our previous analyses for one or more of the biomarkers, and with demonstrated involvement in AD. We found that gray matter regions such as hippocampal [106], parasubiculum [107], entorhinal [108], retrosplenial [109] and

Author Manuscript Author Manuscript Author Manuscript Author Manuscript

motor cortices provided good predictions for spatial memory performance. While our techniques were limited in resolution to 100 μm, we were able to identify the fornix volume, and QSM as predictors for spatial memory function. Other white matter tracts such as the anterior commissure (connecting the temporal lobe structures), and corpus callosum (largely responsible for interhemispheric connectivity) may need to be investigated in future studies. Such studies may help understand how disease propagation within brain networks leads to cognitive deterioration.

Finally, we assessed the value of individual and combined imaging biomarkers in predicting spatial memory for whole brain based analyses, and for selected regions which appeared as eigen solutions for one or more imaging markers and had demonstrated roles in AD. We found that the combined supervised approach improved the prediction accuracy relative to single biomarkers, in agreement with [25] [26] [110].

A limitation of our approach comes from the small sample size, a problem that is common to many preclinical studies. This restricts us to using simpler models. However, this is alleviated by the genetic similarity of mouse populations relative to clinical populations. While in this study we demonstrated a promising approach for predictive modeling in mouse models of AD, future studies would benefit from larger samples. Such studies may test other correlatives, and attempt to build genotype specific models.

Possible neurotoxic effects may limit manganese studies, in particular their applicability to longitudinal studies in animal models, and they are certainly not amenable to human studies. To maximize contrast while reducing toxicity, we chose a small but continuous delivery method, via implanted mini-pumps, over a single injection [111]. An additional consideration when using QSM in manganese dosed models of AD is the possibility of compound effects, e.g. iron accumulation, which is likely to dominate in effect size, and may induce oxidative tissue damage [112] [113]. However, our technique produced QSM with exquisite contrast by exploiting the MR phase, in addition to providing morphometry and T1wMEMRI signal information. This approach holds promise as a more direct measure of functional information based on imaging [114] [115].

Since imaging biomarkers may indicate changes before overt cognitive decline [116], such approaches can help with early diagnosis and patient stratification. It would be interesting to include vascular biomarkers, which may constitute early events in fronto-temporal dementia [116] and AD [117]. Future studies may address predictions along a temporal scale, and give insight into the dynamics of interactions among pathological factors, in relation to disease propagation.

To the best of our knowledge this is the first application of sparse predictive modeling integrating multivariate biomarkers for structure and brain activity, to map circuits responsible for behavioral dysfunction in models of AD. Mapping cognition to brain circuits will increasingly rely on such multivariate statistical algorithms involving clustering, module detection, or other dimensionality reduction approaches, which offer increased power to identify signatures of neurodegenerative disease. The success of such translational approaches will allow testing mechanistic hypotheses using mouse models and help develop

Author Manuscript Author Manuscript Author Manuscript Author Manuscript

better models for complex diseases. In conclusion, we show that MEMRI can both enhance contrast and thus contribute to the increased accuracy of volume measurements, as well as provide a tool for studying brain dysfunction in rodent models of neurological disorders.

Our approach synergized information from multivariate imaging and behavioral markers, allowing for observation of multifactorial biological processes and enabling future modeling of such factor-factor interactions, locally or as they spread over physical brain networks, to alter functional networks and ultimately cognition. Our results demonstrated that integrative predictive modeling approaches may outperform any single one imaging modality, giving us the ability to map vulnerable brain circuits responsible for cognitive changes, including memory deficits. This is in particular important for a multifactorial disease like AD, where the same regions are affected by multiple pathologies. Moreover, such multivariate approaches hold promise to help discover mechanistic links between the structural and functional components of brain circuits that underlie cognitive dysfunction in AD.

Supplementary Material

Refer to Web version on PubMed Central for supplementary material.

Acknowledgments

Imaging was performed at the Center for In Vivo Microscopy (CIVM), supported through P41 EB015897 (G Allan Johnson). We thank all CIVM-ers for their efforts to build and maintain this resource, and a collaborative learning environment. We thank Angela Everhart for help with histological staining. We thank William Kirby Gottschalk, Michael Lutz, Sayan Mukherjee and Nian Wang for helpful discussions, John Nouls for maintaining the 7 T magnet; Gary Cofer for generously sharing his MR knowledge with students, James Cook and Lucy Upchurch for supporting the computing resources. We thank Ramona Rodriguiz and Christopher Means for help with behavioral assays. The behavior testing was done on instruments acquired with support from the NC Biotechnology Fund. This work was supported by the National Institutes of Health through K01 AG041211 (Badea), R01 AG045422 (Colton), R56 AG051765 (Colton), R56 AG 057895 (Colton, Badea, et al.).

References

1. Bartus RT, et al., The cholinergic hypothesis of geriatric memory dysfunction. Science, 1982 217(4558): p. 408–417. [PubMed: 7046051]
2. Braak H and Braak E, Neuropathological stageing of Alzheimer-related changes. Acta Neuropathologica, 1991 82(4): p. 239–259. [PubMed: 1759558]
3. Serrano-Pozo A, et al., Neuropathological alterations in Alzheimer disease. Cold Spring Harbor Perspectives in Medicine, 2011 1(1): p. a006189. [PubMed: 22229116]
4. Knopman D, et al., Cardiovascular risk factors and cognitive decline in middle-aged adults. Neurology, 2001 56(1): p. 42–48. [PubMed: 11148234]
5. Gorelick PB, et al., Vascular contributions to cognitive impairment and dementia: A statement for healthcare professionals from the American Heart Association/American Stroke Association. Stroke, 2011 42(9): p. 2672–2713. [PubMed: 21778438]
6. Talbot K, et al., Demonstrated brain insulin resistance in Alzheimer's disease patients is associated with IGF-1 resistance, IRS-1 dysregulation, and cognitive decline. Journal of Clinical Investigation, 2012 122(4): p. 1316–1338. [PubMed: 22476197]
7. Arvanitakis Z, et al., Diabetes Mellitus and Risk of Alzheimer Disease and Decline in Cognitive Function. Archives of Neurology, 2004 61(5): p. 661–666. [PubMed: 15148141]
8. Block ML, Zecca L, and Hong JS, Microglia-mediated neurotoxicity: Uncovering the molecular mechanisms. Nature Reviews Neuroscience, 2007 8(1): p. 57–69. [PubMed: 17180163]

Author Manuscript Author Manuscript Author Manuscript Author Manuscript

9. Heneka MT, et al., Neuroinflammation in Alzheimer's disease. The Lancet Neurology, 2015 14(4): p. 388–405. [PubMed: 25792098]
10. Goldman-Rakic PS, Topography of cognition: parallel distributed networks in primate association cortex. Annu Rev Neurosci, 1988 11: p. 137–56. [PubMed: 3284439]
11. Buckner RL, Andrews-Hanna JR, and Schacter DL, The brain's default network: Anatomy, function, and relevance to disease, in Annals of the New York Academy of Sciences. 2008 p. 1–38.
12. Smith SM, et al., Correspondence of the brain's functional architecture during activation and rest. Proc Natl Acad Sci U S A, 2009 106(31): p. 13040–5. [PubMed: 19620724]
13. Celone KA, et al., Alterations in memory networks in mild cognitive impairment and Alzheimer's disease: An independent component analysis. Journal of Neuroscience, 2006 26(40): p. 10222–10231. [PubMed: 17021177]
14. Folstein MF, Folstein SE, and McHugh PR, "Mini-mental state". Journal of Psychiatric Research, 1975 12(3): p. 189–198. [PubMed: 1202204]
15. Nasreddine ZS, et al., The Montreal Cognitive Assessment, MoCA: a brief screening tool for mild cognitive impairment. J Am Geriatr Soc, 2005 53(4): p. 695–9. [PubMed: 15817019]
16. Cummings JL, et al., The neuropsychiatric inventory: Comprehensive assessment of psychopathology in dementia. Neurology, 1994 44(12): p. 2308–2314. [PubMed: 7991117]
17. Thompson PM, et al., Dynamics of gray matter loss in Alzheimer's disease. Journal of Neuroscience, 2003 23(3): p. 994–1005. [PubMed: 12574429]
18. Lehmann M, et al., Diverging patterns of amyloid deposition and hypometabolism in clinical variants of probable Alzheimer's disease. Brain, 2013 136(Pt 3): p. 844–58. [PubMed: 23358601]
19. Slattery CF, et al., ApoE influences regional white-matter axonal density loss in Alzheimer's disease. Neurobiology of Aging, 2017 57: p. 8–17. [PubMed: 28578156]
20. Ossenkoppele R, et al., Atrophy patterns in early clinical stages across distinct phenotypes of Alzheimer's disease. Human Brain Mapping, 2015 36(11): p. 4421–4437. [PubMed: 26260856]
21. Ossenkoppele R, et al., Tau PET patterns mirror clinical and neuroanatomical variability in Alzheimer's disease. Brain, 2016 139(5): p. 1551–1567. [PubMed: 26962052]
22. Whitwell JL, et al., 3D maps from multiple MRI illustrate changing atrophy patterns as subjects progress from mild cognitive impairment to Alzheimer's disease. Brain, 2007 130(Pt 7): p. 1777–86. [PubMed: 17533169]
23. Holland D, et al., Subregional neuroanatomical change as a biomarker for Alzheimer's disease. Proceedings of the National Academy of Sciences of the United States of America, 2009 106(49): p. 20954–20959. [PubMed: 19996185]
24. Woo CW, et al., Building better biomarkers: brain models in translational neuroimaging. Nat Neurosci, 2017 20(3): p. 365–377. [PubMed: 28230847]
25. Avants B, et al., Eigenanatomy improves detection power for longitudinal cortical change. Med Image Comput Comput Assist Interv, 2012 15(Pt 3): p. 206–13.
26. Kandel BM, et al., Predicting cognitive data from medical images using sparse linear regression. Inf Process Med Imaging, 2013 23: p. 86–97. [PubMed: 24683960]
27. Hsiao K, et al., Correlative memory deficits, Abeta elevation, and amyloid plaques in transgenic mice. Science, 1996 274(5284): p. 99–102. [PubMed: 8810256]
28. Duff K, et al., Increased amyloid-beta42(43) in brains of mice expressing mutant presenilin 1. Nature, 1996 383(6602): p. 710–3. [PubMed: 8878479]
29. Holcomb L, et al., Accelerated Alzheimer-type phenotype in transgenic mice carrying both mutant amyloid precursor protein and presenilin 1 transgenes. Nat Med, 1998 4(1): p. 97–100. [PubMed: 9427614]
30. Oddo S, et al., Triple-transgenic model of Alzheimer's disease with plaques and tangles: intracellular Abeta and synaptic dysfunction. Neuron, 2003 39(3): p. 409–21. [PubMed: 12895417]
31. Franco R, Martínez-Pinilla E, and Navarro G, Why have transgenic rodent models failed to successfully mimic Alzheimer's disease. How can we develop effective drugs without them? Expert Opinion on Drug Discovery, 2019 14(4): p. 327–330. [PubMed: 30775940]

Author Manuscript Author Manuscript Author Manuscript Author Manuscript

32. Gong JS, et al., Apolipoprotein E (ApoE) isoform-dependent lipid release from astrocytes prepared from human ApoE3 and ApoE4 knock-in mice. The Journal of biological chemistry, 2002 277(33): p. 29919–29926. [PubMed: 12042316]
33. Roses AD, et al., Morphological, biochemical, and genetic support for an apolipoprotein E effect on microtubular metabolism, in Annals of the New York Academy of Sciences. 1996 p. 146–157.
34. Knouff C, et al., Apo E structure determines VLDL clearance and atherosclerosis risk in mice. J Clin Invest, 1999 103(11): p. 1579–86. [PubMed: 10359567]
35. Andrews-Zwilling Y, et al., Apolipoprotein E4 causes age- and Tau-dependent impairment of GABAergic interneurons, leading to learning and memory deficits in mice. Journal of Neuroscience, 2010 30(41): p. 13707–13717. [PubMed: 20943911]
36. Hansen DV, Hanson JE, and Sheng M, Microglia in Alzheimer's disease. The Journal of Cell Biology, 2018 217(2): p. 459. [PubMed: 29196460]
37. Hoos MD, et al., The impact of human and mouse differences in NOS2 gene expression on the brain's redox and immune environment. Mol Neurodegener, 2014 9: p. 50. [PubMed: 25403885]
38. Colton CA, et al., The effects of NOS2 gene deletion on mice expressing mutated human AβPP. Journal of Alzheimer's Disease, 2008 15(4): p. 571–587.
39. Kan MJ, et al., Arginine deprivation and immune suppression in a mouse model of Alzheimer's disease. Journal of Neuroscience, 2015 35(15): p. 5969–5982. [PubMed: 25878270]
40. Colton CA, et al., No synthase 2 (NOS2) deletion promotes multiple pathologies in a mouse model of Alzheimer's disease. Proceedings of the National Academy of Sciences of the United States of America, 2006 103(34): p. 12867–12872. [PubMed: 16908860]
41. Wilcock DM, et al., Progression of amyloid pathology to Alzheimer's disease pathology in an amyloid precursor protein transgenic mouse model by removal of nitric oxide synthase 2. J Neurosci, 2008 28(7): p. 1537–45. [PubMed: 18272675]
42. Colton CA, et al., mNos2 deletion and human NOS2 replacement in Alzheimer disease models. J Neuropathol Exp Neurol, 2014 73(8): p. 752–69. [PubMed: 25003233]
43. Kan MJ, et al., Arginine deprivation and immune suppression in a mouse model of Alzheimer's disease. J Neurosci, 2015 35(15): p. 5969–82. [PubMed: 25878270]
44. D'Hooge R and De Deyn PP, Applications of the Morris water maze in the study of learning and memory. Brain Research Reviews, 2001 36(1): p. 60–90. [PubMed: 11516773]
45. Gallagher M, Burwell R, and Burchinal M, Severity of Spatial Learning Impairment in Aging: Development of a Learning Index for Performance in the Morris Water Maze. Behavioral Neuroscience, 1993 107(4): p. 618–626. [PubMed: 8397866]
46. Na HB, et al., Development of a T1 contrast agent for magnetic resonance imaging using MnO nanoparticles. Angewandte Chemie - International Edition, 2007 46(28): p. 5397–5401. [PubMed: 17357103]
47. Aoki I, et al., In vivo detection of neuroarchitecture in the rodent brain using manganese-enhanced MRI. NeuroImage, 2004 22(3): p. 1046–1059. [PubMed: 15219577]
48. Pautler RG, Silva AC, and Koretsky AP, In vivo neuronal tract tracing using manganese-enhanced magnetic resonance imaging. Magnetic Resonance in Medicine, 1998 40(5): p. 740–748. [PubMed: 9797158]
49. Watanabe T, Frahm J, and Michaelis T, Functional mapping of neural pathways in rodent brain in vivo using manganese-enhanced three-dimensional magnetic resonance imaging. NMR in Biomedicine, 2004 17(8): p. 554–568. [PubMed: 15617054]
50. Yu X, et al., In vivo auditory brain mapping in mice with Mn-enhanced MRI. Nature Neuroscience, 2005 8(7): p. 961–968. [PubMed: 15924136]
51. Pautler RG and Koretsky AP, Tracing odor-induced activation in the olfactory bulbs of mice using manganese-enhanced magnetic resonance imaging. NeuroImage, 2002 16(2): p. 441–448. [PubMed: 12030829]
52. Kimura T, et al., Hyperphosphorylated tau in parahippocampal cortex impairs place learning in aged mice expressing wild-type human tau. EMBO Journal, 2007 26(24): p. 5143–5152. [PubMed: 18007595]

Author Manuscript Author Manuscript Author Manuscript Author Manuscript

53. Van der Linden A, et al., Current status of functional MRI on small animals: Application to physiology, pathophysiology, and cognition. NMR in Biomedicine, 2007 20(5): p. 522–545. [PubMed: 17315146]
54. Markesbery WR and Carney JM, Oxidative alterations in Alzheimer's disease. Brain Pathology, 1999 9(1): p. 133–146. [PubMed: 9989456]
55. Jomova K, et al., Metals, oxidative stress and neurodegenerative disorders. Molecular and Cellular Biochemistry, 2010 345(1–2): p. 91–104. [PubMed: 20730621]
56. Avants BB, et al., Dementia induces correlated reductions in white matter integrity and cortical thickness: A multivariate neuroimaging study with sparse canonical correlation analysis. NeuroImage, 2010 50(3): p. 1004–1016. [PubMed: 20083207]
57. Witten DM, Tibshirani R, and Hastie T, A penalized matrix decomposition, with applications to sparse principal components and canonical correlation analysis. Biostatistics, 2009 10(3): p. 515–534. [PubMed: 19377034]
58. Tustison NJ, et al., N4ITK: improved N3 bias correction. IEEE transactions on medical imaging, 2010 29(6): p. 1310–1320. [PubMed: 20378467]
59. Badea A, Ali-Sharief AA, and Johnson GA, Morphometric analysis of the C57BL/6J mouse brain. NeuroImage, 2007 37(3): p. 683–693. [PubMed: 17627846]
60. Johnson GA, et al., Waxholm space: an image-based reference for coordinating mouse brain research. Neuroimage, 2010 53(2): p. 365–372. [PubMed: 20600960]
61. Avants BB, et al., The optimal template effect in hippocampus studies of diseased populations. Neuroimage, 2010 49(3): p. 2457–66. [PubMed: 19818860]
62. Avants BB, et al., An open source multivariate framework for n-tissue segmentation with evaluation on public data. Neuroinformatics, 2011 9(4): p. 381–400. [PubMed: 21373993]
63. Anderson RJ, et al., Small Animal Multivariate Brain Analysis (SAMBA): A High Throughput Pipeline with a Validation Framework. eprint arXiv:1709.10483, 2017: p. arXiv:1709.10483.
64. Calabrese E, et al., A Diffusion MRI Tractography Connectome of the Mouse Brain and Comparison with Neuronal Tracer Data. Cereb Cortex, 2015 25(11): p. 4628–37. [PubMed: 26048951]
65. Leow AD, et al., Statistical properties of Jacobian maps and the realization of unbiased large-deformation nonlinear image registration. IEEE Trans Med Imaging, 2007 26(6): p. 822–32. [PubMed: 17679333]
66. Lin YJ and Koretsky AP, Manganese ion enhances T1-weighted MRI during brain activation: An approach to direct imaging of brain function. Magnetic Resonance in Medicine, 1997 38(3): p. 378–388. [PubMed: 9339438]
67. Li W, et al., Integrated Laplacian-based phase unwrapping and background phase removal for quantitative susceptibility mapping. NMR in biomedicine, 2014 27(2): p. 219–227. [PubMed: 24357120]
68. Wu B, et al., Whole brain susceptibility mapping using compressed sensing. Magnetic Resonance in Medicine, 2012 67(1): p. 137–147. [PubMed: 21671269]
69. Wei H, et al., Streaking artifact reduction for quantitative susceptibility mapping of sources with large dynamic range. NMR Biomed, 2015 28(10): p. 1294–303. [PubMed: 26313885]
70. Friston KJ, et al., Assessing the significance of focal activations using their spatial extent. Hum Brain Mapp, 1994 1(3): p. 210–20. [PubMed: 24578041]
71. Avants BB, et al., Sparse canonical correlation analysis relates network-level atrophy to multivariate cognitive measures in a neurodegenerative population. NeuroImage, 2014 84: p. 698–711. [PubMed: 24096125]
72. Bengio Y and Grandvalet Y, No unbiased estimator of the variance of K-fold cross-validation. Journal of Machine Learning Research, 2004 5: p. 1089–1105.
73. Selkoe DJ, Alzheimer's disease: Genotypes, phenotype, and treatments. Science, 1997 275(5300): p. 630–631. [PubMed: 9019820]
74. Näslund J, et al., Correlation between elevated levels of amyloid β-peptide in the brain and cognitive decline. Journal of the American Medical Association, 2000 283(12): p. 1571–1577. [PubMed: 10735393]

Author Manuscript Author Manuscript Author Manuscript Author Manuscript

75. Micotti E, et al., Striatum and entorhinal cortex atrophy in AD mouse models: MRI comprehensive analysis. Neurobiol Aging, 2015 36(2): p. 776–88. [PubMed: 25433456]
76. Badea A, et al., The fornix provides multiple biomarkers to characterize circuit disruption in a mouse model of Alzheimer's disease. Neuroimage, 2016 142: p. 498–511. [PubMed: 27521741]
77. Hotelling H, Relations between two sets of variates. Biometrika, 1936 28(3/4): p. 321–377.
78. Tibshirani R, Regression shrinkage and selection via the lasso. Journal of the Royal Statistical Society Series B (Methodological) 1996 58(1): p. 267–288
79. Dhillon PS, et al., Subject-specific functional parcellation via prior based eigenanatomy. Neuroimage, 2014 99(1095–9572 (Electronic)): p. 14–27. [PubMed: 24852460]
80. Pistorio AL, Hendry SH, and Wang X, A modified technique for high-resolution staining of myelin. J Neurosci Methods, 2006 153(1): p. 135–46. [PubMed: 16310256]
81. Iturria-Medina Y, et al., Early role of vascular dysregulation on late-onset Alzheimer's disease based on multifactorial data-driven analysis. Nat Commun, 2016 7: p. 11934. [PubMed: 27327500]
82. Hsiao K, et al., Correlative memory deficits, Aβ elevation, and amyloid plaques in transgenic mice. Science, 1996 274(5284): p. 99–102. [PubMed: 8810256]
83. Chishti MA, et al., Early-onset Amyloid Deposition and Cognitive Deficits in Transgenic Mice Expressing a Double Mutant Form of Amyloid Precursor Protein 695. Journal of Biological Chemistry, 2001 276(24): p. 21562–21570. [PubMed: 11279122]
84. Lesné S, et al., A specific amyloid-β protein assembly in the brain impairs memory. Nature, 2006 440(7082): p. 352–357. [PubMed: 16541076]
85. Westerman MA, et al., The relationship between Aβ and memory in the Tg2576 mouse model of Alzheimer's disease. Journal of Neuroscience, 2002 22(5): p. 1858–1867. [PubMed: 11880515]
86. Roberson ED, et al., Reducing endogenous tau ameliorates amyloid β-induced deficits in an Alzheimer's disease mouse model. Science, 2007 316(5825): p. 750–754. [PubMed: 17478722]
87. Saura CA, et al., Loss of presenilin function causes impairments of memory and synaptic plasticity followed by age-dependent neurodegeneration. Neuron, 2004 42(1): p. 23–36. [PubMed: 15066262]
88. Watanabe T, et al., In vivo 3D MRI staining of mouse brain after subcutaneous application of MnCl2. Magnetic Resonance in Medicine, 2002 48(5): p. 852–859. [PubMed: 12418000]
89. Silva AC, et al., Manganese-enhanced magnetic resonance imaging (MEMRI): methodological and practical considerations. NMR Biomed, 2004 17(8): p. 532–43. [PubMed: 15617052]
90. Kuo YT, et al., Manganese-enhanced magnetic resonance imaging (MEMRI) without compromise of the blood-brain barrier detects hypothalamic neuronal activity in vivo. NMR in Biomedicine, 2006 19(8): p. 1028–1034. [PubMed: 16845705]
91. Perez PD, et al., In vivo functional brain mapping in a conditional mouse model of human tauopathy (tau p301l) reveals reduced neural activity in memory formation structures. Molecular Neurodegeneration, 2013 8(1): p. 9. [PubMed: 23379588]
92. Tang X, et al., Spatial learning and memory impairments are associated with increased neuronal activity in 5XFAD mouse as measured by manganese-enhanced magnetic resonance imaging. Oncotarget, 2016 7(36): p. 57556–57570. [PubMed: 27542275]
93. Ameen-Ali KE, et al., Review: Neuropathology and behavioural features of transgenic murine models of Alzheimer's disease. Neuropathol Appl Neurobiol, 2017 43(7): p. 553–570. [PubMed: 28880417]
94. Kirsch W, et al., Serial susceptibility weighted MRI measures brain iron and microbleeds in dementia. J Alzheimers Dis, 2009 17(3): p. 599–609. [PubMed: 19433895]
95. Ayton S, et al., Cerebral quantitative susceptibility mapping predicts amyloid-β-related cognitive decline. Brain, 2017 140(8): p. 2112–2119. [PubMed: 28899019]
96. Hoffstaedter F, et al., The role of anterior midcingulate cortex in cognitive motor control: evidence from functional connectivity analyses. Human brain mapping, 2014 35(6): p. 2741–2753. [PubMed: 24115159]
97. Weible AP, et al., Neural correlates of long-term object memory in the mouse anterior cingulate cortex. J Neurosci, 2012 32(16): p. 5598–608. [PubMed: 22514321]

Author Manuscript Author Manuscript Author Manuscript Author Manuscript

98. Allemang-Grand R, et al., Altered brain development in an early-onset murine model of Alzheimer's disease. Neurobiol Aging, 2015 36(2): p. 638–47. [PubMed: 25311279]

99. Grand'maison M, et al., Early cortical thickness changes predict beta-amyloid deposition in a mouse model of Alzheimer's disease. Neurobiol Dis, 2013 54: p. 59–67. [PubMed: 23454197]

100. Grandjean J, et al., Complex interplay between brain function and structure during cerebral amyloidosis in APP transgenic mouse strains revealed by multi-parametric MRI comparison. Neuroimage, 2016 134: p. 1–11. [PubMed: 27033685]

101. Ewers M, et al., Neuroimaging markers for the prediction and early diagnosis of Alzheimer's disease dementia. Trends Neurosci, 2011 34(8): p. 430–42. [PubMed: 21696834]

102. Gispert JD, et al., Nonlinear cerebral atrophy patterns across the Alzheimer's disease continuum: impact of APOE4 genotype. Neurobiol Aging, 2015 36(10): p. 2687–701. [PubMed: 26239178]

103. Fortea J, et al., Increased cortical thickness and caudate volume precede atrophy in PSEN1 mutation carriers. J Alzheimers Dis, 2010 22(3): p. 909–22. [PubMed: 20858974]

104. Beach TG, Walker R, and McGeer EG, Patterns of gliosis in Alzheimer's disease and aging cerebrum. Glia, 1989 2(6): p. 420–36. [PubMed: 2531723]

105. Iacono D, et al., Neuronal hypertrophy in asymptomatic Alzheimer disease. J Neuropathol Exp Neurol, 2008 67(6): p. 578–89. [PubMed: 18520776]

106. Bohbot VD, et al., Gray matter differences correlate with spontaneous strategies in a human virtual navigation task. J Neurosci, 2007 27(38): p. 10078–83. [PubMed: 17881514]

107. Kesner RP and Giles R, Neural circuit analysis of spatial working memory: role of pre- and parasubiculum, medial and lateral entorhinal cortex. Hippocampus, 1998 8(4): p. 416–23. [PubMed: 9744426]

108. Sasaki T, Leutgeb S, and Leutgeb JK, Spatial and memory circuits in the medial entorhinal cortex. Curr Opin Neurobiol, 2015 32: p. 16–23. [PubMed: 25463560]

109. Vann SD, Aggleton JP, and Maguire EA, What does the retrosplenial cortex do? Nat Rev Neurosci, 2009 10(11): p. 792–802. [PubMed: 19812579]

110. Kandel BM, et al., Eigenanatomy: sparse dimensionality reduction for multi-modal medical image analysis. Methods, 2015 73: p. 43–53. [PubMed: 25448483]

111. Poole DS, et al., Continuous infusion of manganese improves contrast and reduces side effects in manganese-enhanced magnetic resonance imaging studies. NeuroImage, 2017 147: p. 1–9. [PubMed: 27777173]

112. Lovell MA, et al., Copper, iron and zinc in Alzheimer's disease senile plaques. Journal of the Neurological Sciences, 1998 158(1): p. 47–52. [PubMed: 9667777]

113. Zecca L, et al., Iron, brain ageing and neurodegenerative disorders. Nature Reviews Neuroscience, 2004 5(11): p. 863–873. [PubMed: 15496864]

114. Baxan N, et al., Microcoil-based MR phase imaging and manganese enhanced microscopy of glial tumor neurospheres with direct optical correlation. Magn Reson Med, 2012 68(1): p. 86–97. [PubMed: 22127877]

115. Balla DZ, et al., Functional quantitative susceptibility mapping (fQSM). Neuroimage, 2014 100: p. 112–24. [PubMed: 24945672]

116. Olm CA, et al., Arterial spin labeling perfusion predicts longitudinal decline in semantic variant primary progressive aphasia. J Neurol, 2016 263(10): p. 1927–38. [PubMed: 27379517]

117. Iturria-Medina Y, et al., Multifactorial causal model of brain (dis)organization and therapeutic intervention: Application to Alzheimer's disease. Neuroimage, 2017 152: p. 60–77. [PubMed: 28257929]

Author Manuscript Author Manuscript Author Manuscript Author Manuscript

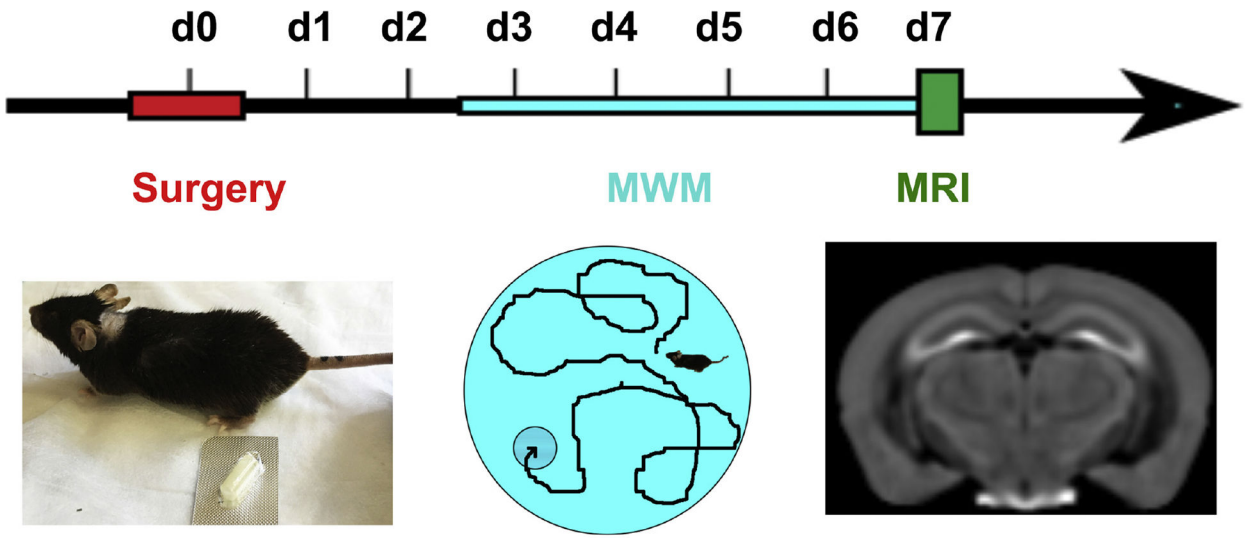

Figure 1. Experimental timeline.

Each animal was implanted with a $MnCl_2$ filled minipump on day 0 (d0), then acclimated for 3 days. Behavior was assessed over 5 days (d3-d7) using the Morris Water Maze (MWM). Subsequently mice were imaged using *in vivo* MRI.

Author Manuscript Author Manuscript Author Manuscript Author Manuscript

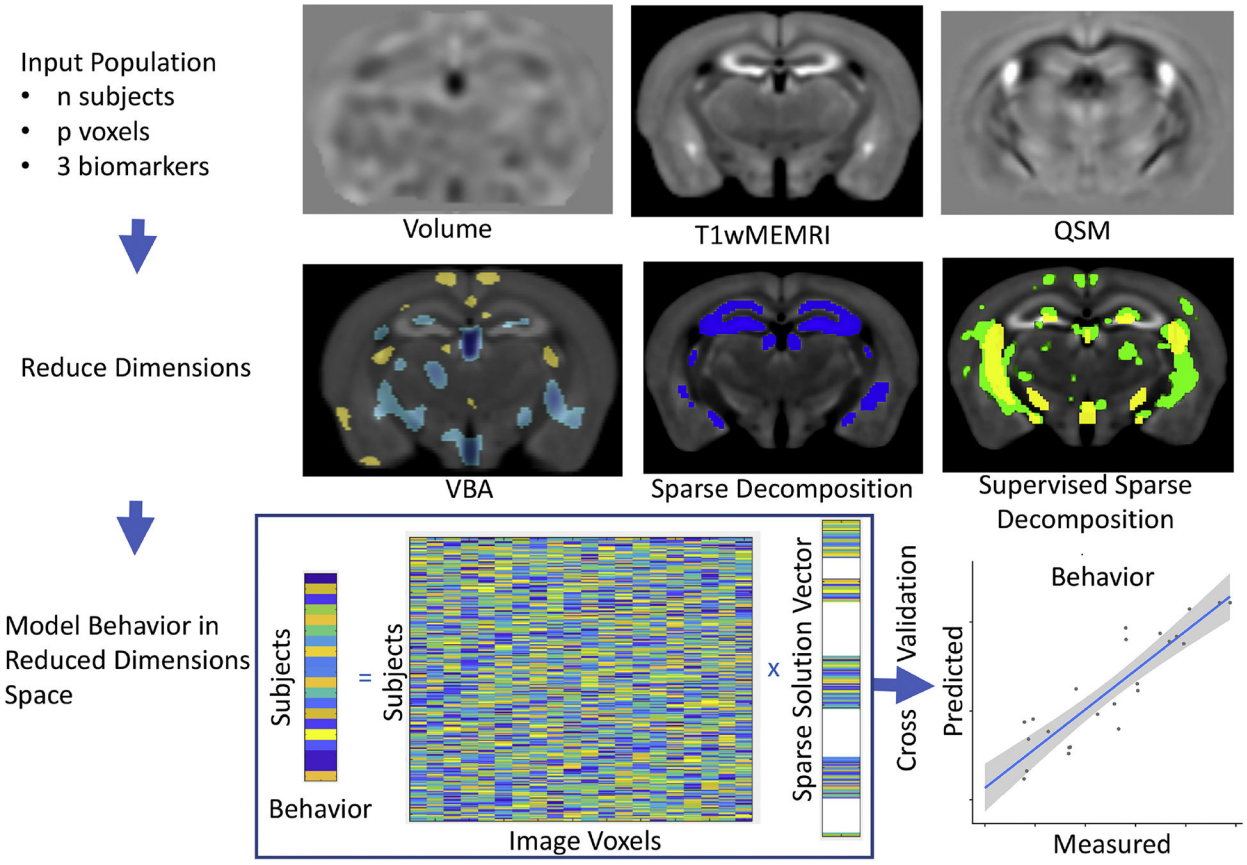

Figure 2. Schematic of the modeling approach.

We start with an image space representation for each of the subjects. This is converted into a reduced dimensionality space, where we model behavior using weights for the sparse solution vectors.

Author Manuscript Author Manuscript Author Manuscript Author Manuscript

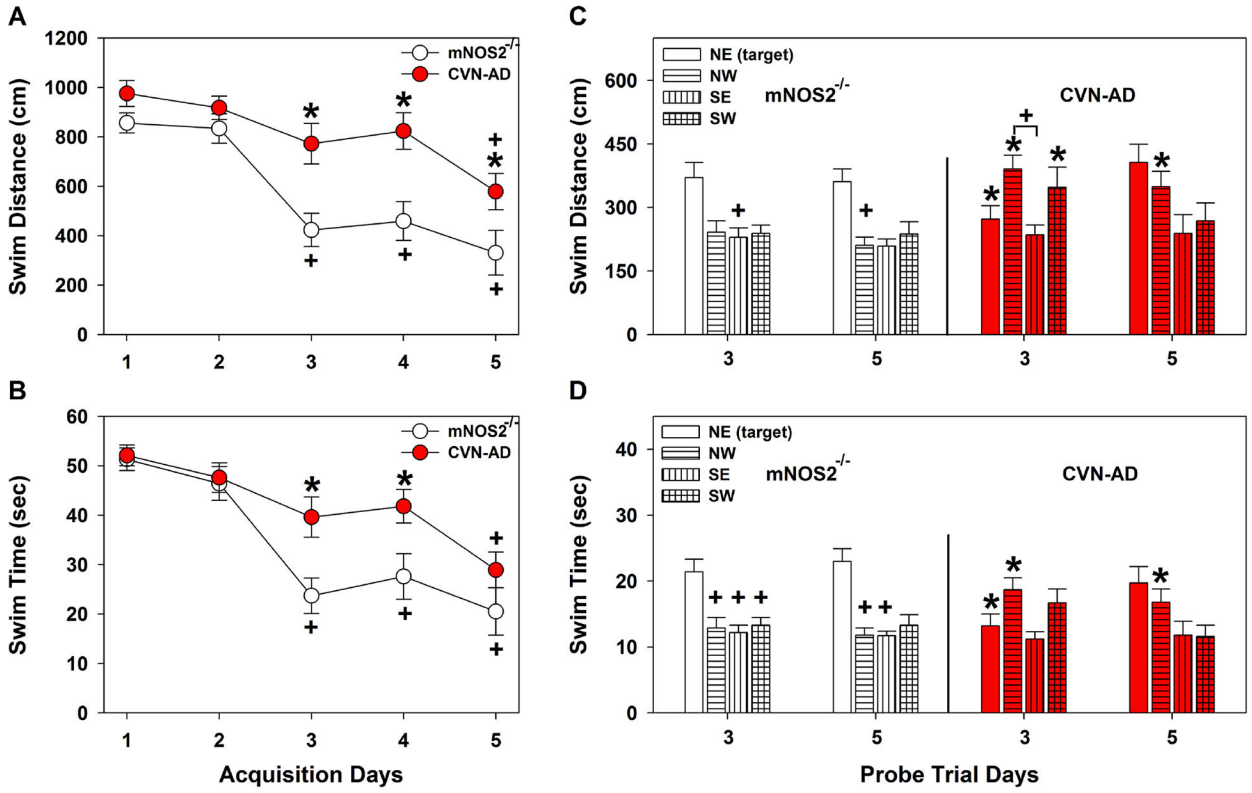

Figure 3.

Main results for the acquisition performance and probe trial results (mean± SEM). (A) Repeated measures ANOVA (RMANOVA) for swim distance during acquisition testing for the Morris water maze detected a significant within subjects main effect of time [F(4,88)=22.436, p<0.001] and a significant time by genotype interaction [F(4,88)=2.451, p=0.012]; the between subjects effect of genotype was significant also [F(1,22)=13.229, p<0.001]. (B) RMANOVA for swim time during acquisition testing noted that the within subjects main effect of time [F(4,88)=26.706, p<0.001], the time by genotype interaction [F(4,88)=2.667, p=0.037], and the between subjects effect of genotype [F(1,22)=5.466, p=0.029] were all significant. N=13 *m*Nos2−/− mice and N=11 CVN-AD mice. (C) For the probe trial RMANOVA differences in swim distance between groups within test day and maze zone identified a trend for the day by zone by genotype interaction [F(3,63)=2.241, p=0.092]. The within subjects contrasts however revealed significant linear effects of zone [F(1,21)=11.924, p<0.002) and cubic effects for zone by genotype interaction [F(1,21)=10.783, p=0.004)]. While the test day, test day by genotype and test day by zone interactions were not significant, the three way test day by zone by genotype interaction was found to be significant by linear within subjects contracts [F(1,21)=4.292, p<0.051]. Moreover, the between subjects effects for genotype alone were also significant [F(1,21)=17.441, p<0.001]. (D) Similar effects were found for the probe trial with swim time where RMANOVA only found the main effect of zone [F(3,63)=11.74, p<0.001] and the zone by genotype interaction [F(3,63)=5.79, p=0.001] to be significant. Within subjects contrasts for Zone [F(1,21)=16.117, p<0.001], and zone by genotype interaction [F(1,21)=9.071, p<0.001] were significant. The three way test day by genotype by zone

Author Manuscript Author Manuscript Author Manuscript Author Manuscript

were found to approach significance [$F(1,21)=3.093$, $p<0.093$). Note that the control mice had a strong preference for the target quadrant, while this was less clear for CVNAD mice, as illustrated in text. NE=northeast (target quadrant), NW=northwest, SE=southeast, SW=southwest. Note, one mNos2−/− control was not tested on the probe trial day 5 due to a lesion. N=12 mNos2−/− mice and N=11 CVN-AD mice; *$p<0.05$, mNos2−/− versus CVN-AD mice; +$p<0.05$, within genotype versus day 1 acquisition trials (A, B); +$p<0.05$, within genotype comparisons versus target quadrant (C, D).

Author Manuscript Author Manuscript Author Manuscript Author Manuscript

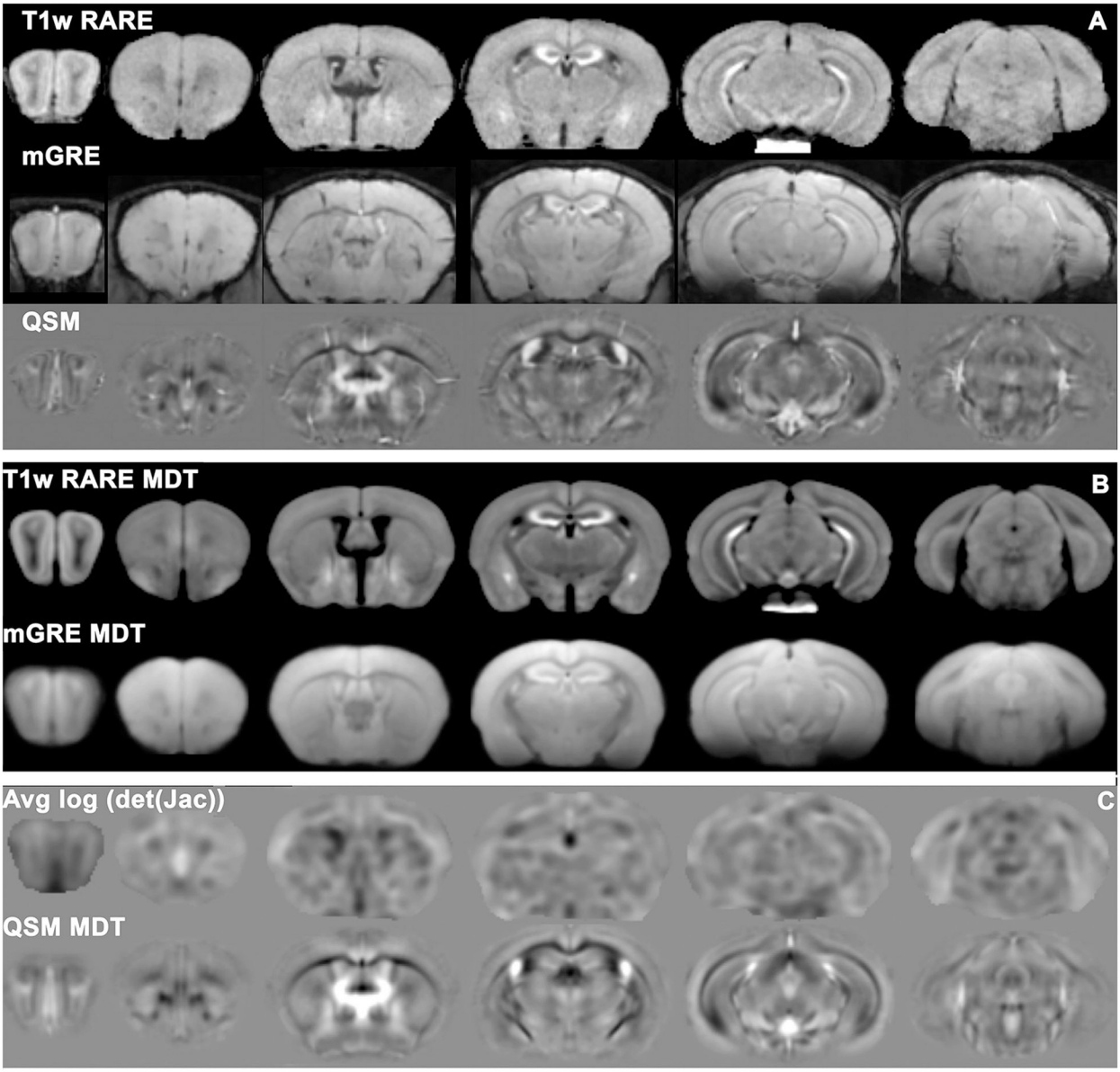

Figure 4. T1-weighted RARE and mGRE images were acquired for 24 mice, and the mGRE was used to calculate quantitative susceptibility maps (QSM).

Representative images from one mouse are shown in (A). The control group was used to calculate minimum deformation templates (MDT) (B) for T1wMEMRI RARE and mGRE images, to produce the deformation maps (C), and MDT for QSM (D).

Author Manuscript Author Manuscript Author Manuscript Author Manuscript

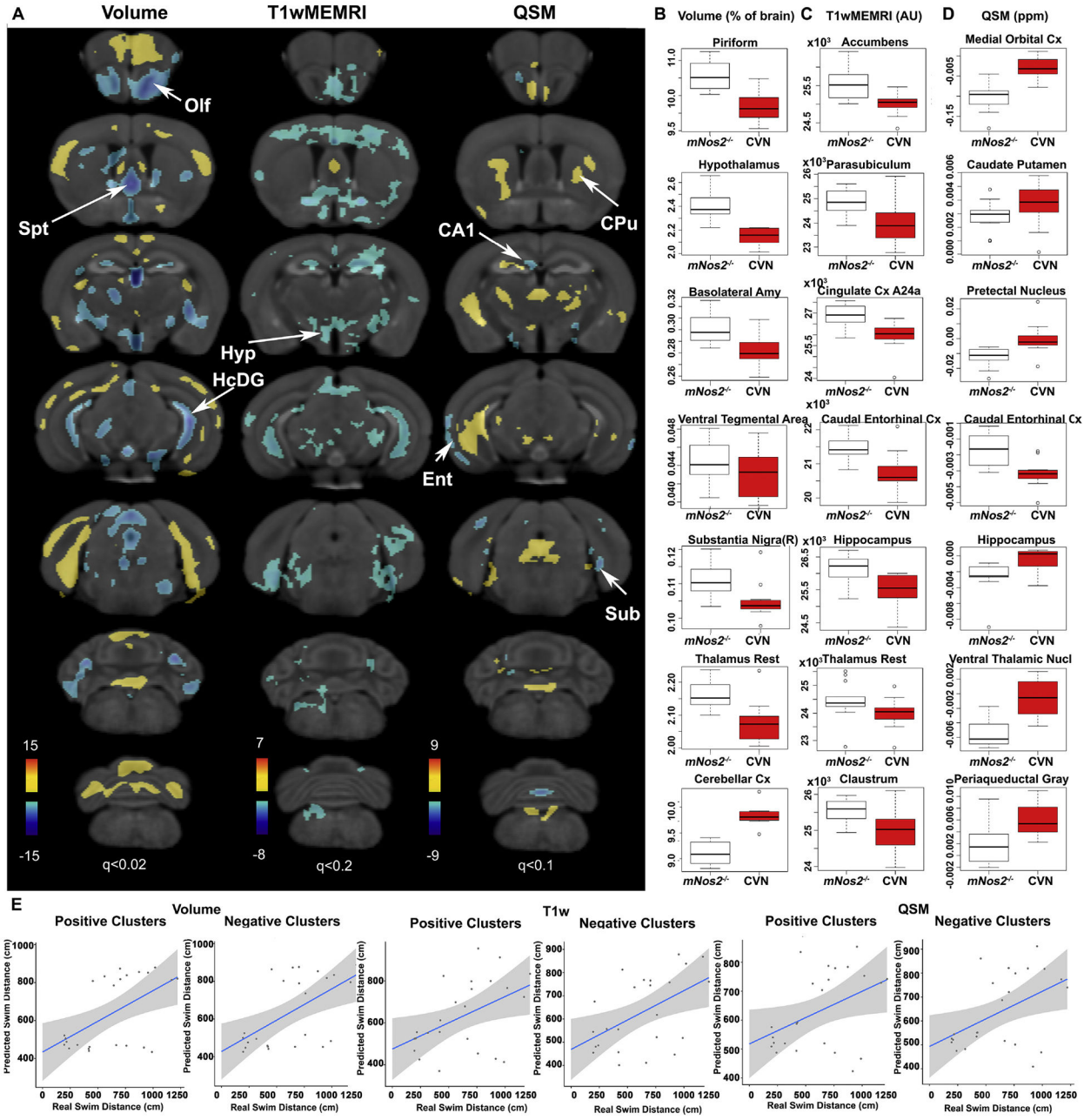

Figure 5. (A) Voxel-based analysis (VBA) identified genotype differences in all three biomarkers (volume, T1-weigted MEMRI signal, and susceptibility).

Statistical t maps were thresholded using false discovery rate (q). Regional properties identified areas of significant differences for (B) volume; (C) T1wMEMRI signal intensity normalized to total brain; (D) magnetic susceptibility (QSM). Local atrophy was evident in the olfactory areas (Olf), septum (Spt), and dentate gyrus of the hippocampus (HcDG) in the CVN-AD model. Manganese uptake was lower in these mice, with the exception for the septum/fornix. Susceptibility was increased in the olfactory areas, caudate putamen (CPu), and dentate gyrus of hippocampus, but decreased in the CA1, entorhinal cortex (Ent), and

subiculum (Sub). (E) VBA identified regions were used for predicting behavior, based on regions with either positive or negative effects for volume, T1wMEMRI signal, and QSM.

Author Manuscript Author Manuscript Author Manuscript Author Manuscript

Author Manuscript Author Manuscript Author Manuscript Author Manuscript

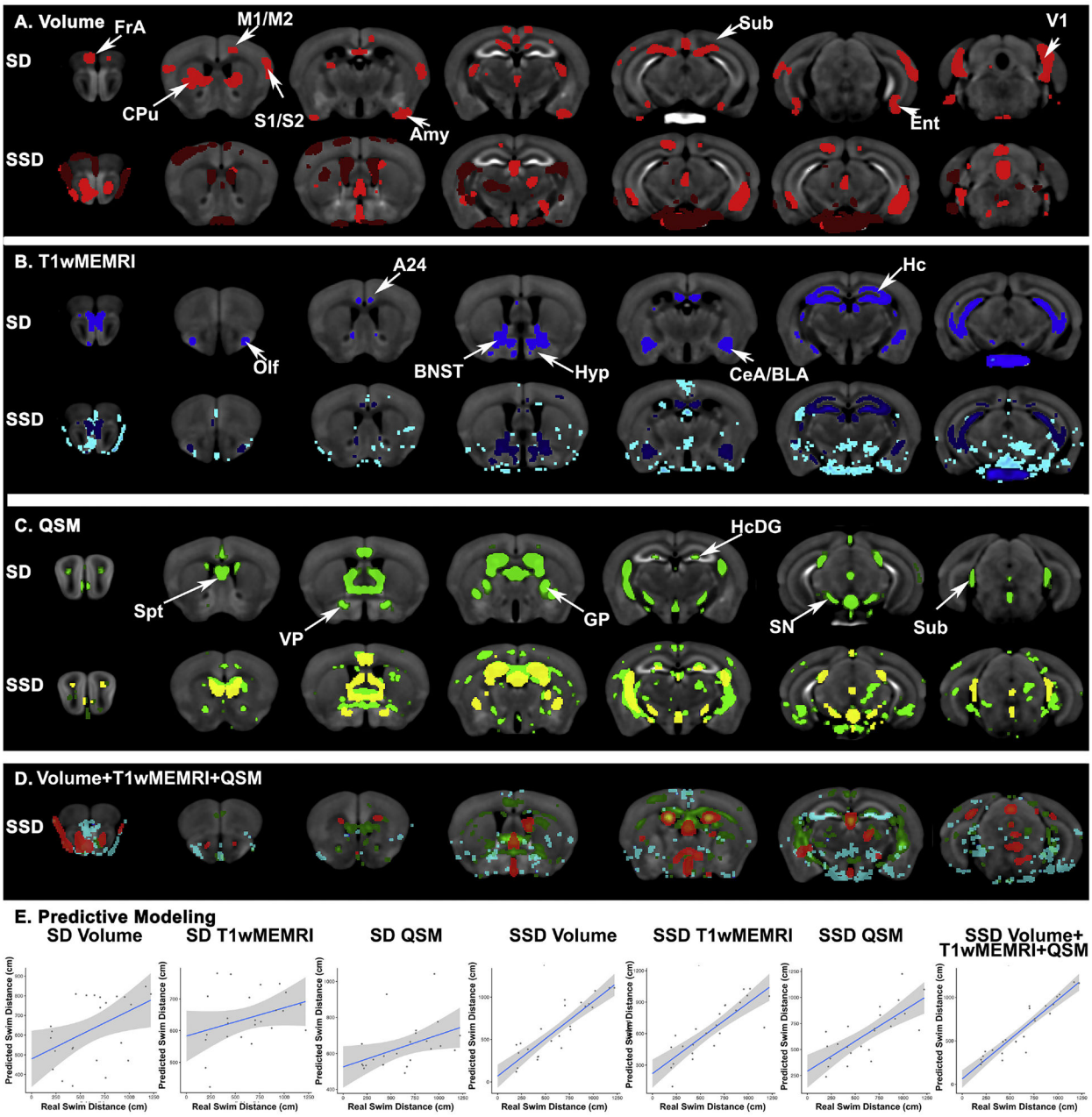

Figure 6. Using volume (A), T1wMEMRI signal (B), QSM (C), or combination of the three biomarkers (D) as predictors we identified significant associations between eigen regions (red for volume, blue for T1wMEMRI and swim distance on day 4.

For all contrasts, the 1st row represents the networks identified by the sparse decomposition. The 2nd row represents the networks identified based on a behavior supervised decomposition. The predictive modeling results for swim distance are shown together with the associated confidence intervals for each of the biomarkers, as well as for the combined approach (E). Our results suggest the integrative approach has increased value when applied to a model of a complex, multifactorial disease such as AD. FrA: frontal association cortex; M1/M2 primary and secondary cortices; CPu: caudate putamen; S1/S2 primary and secondary cortices; Amy: amygdala; Sub: subiculum; Ent: entorhinal cortex; V1: primary

visual cortex; Olf: olfactory areas; A24 cingulate cortex, area 24; BNST: bed nucleus of stria terminalis; Hyp: hypothalamus; CeA: central amygdaloid nucleus; BLA: basolateral amygdala; Hc: hippocampus; Spt: septum; VP: ventral pallium; GP: globus pallidus; Hc:DG: hippocampal dentate gyrus; SN: susbtantia nigra.

Author Manuscript Author Manuscript Author Manuscript Author Manuscript

Author Manuscript Author Manuscript Author Manuscript Author Manuscript

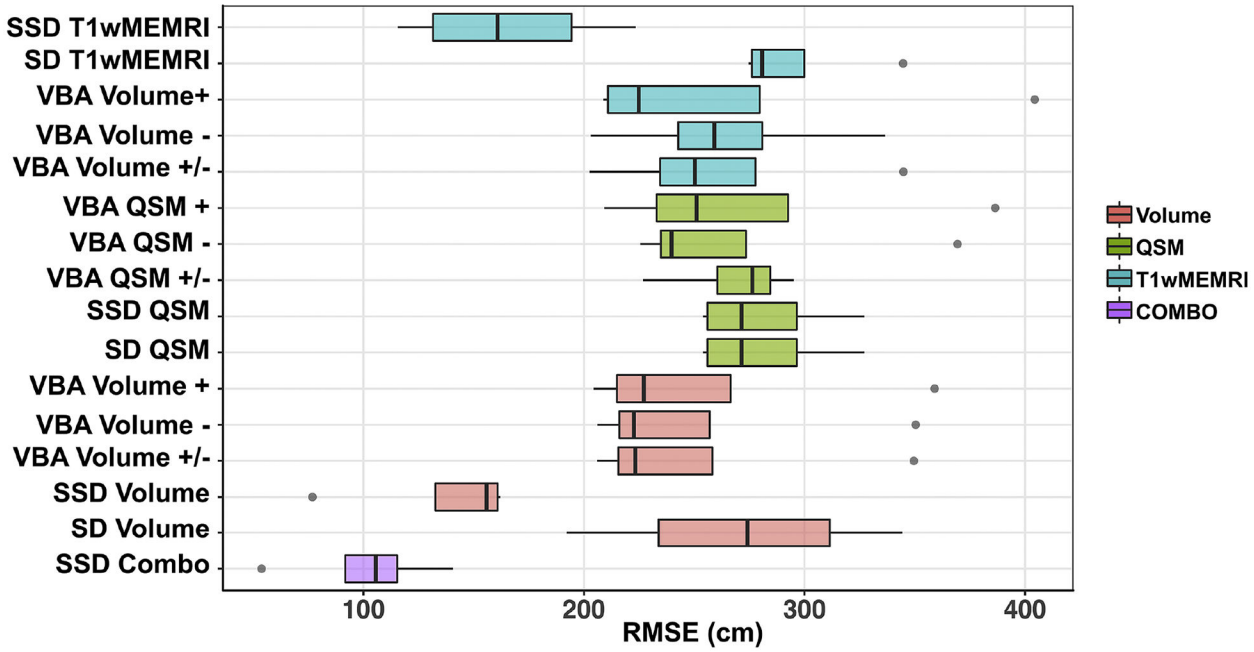

Figure 7.

Model performance comparison based on a whole brain unbiased analysis, showing the root mean square error (RMSE) between the predictions and the true values for the swim distance produced for the 16 models.

Author Manuscript Author Manuscript Author Manuscript Author Manuscript

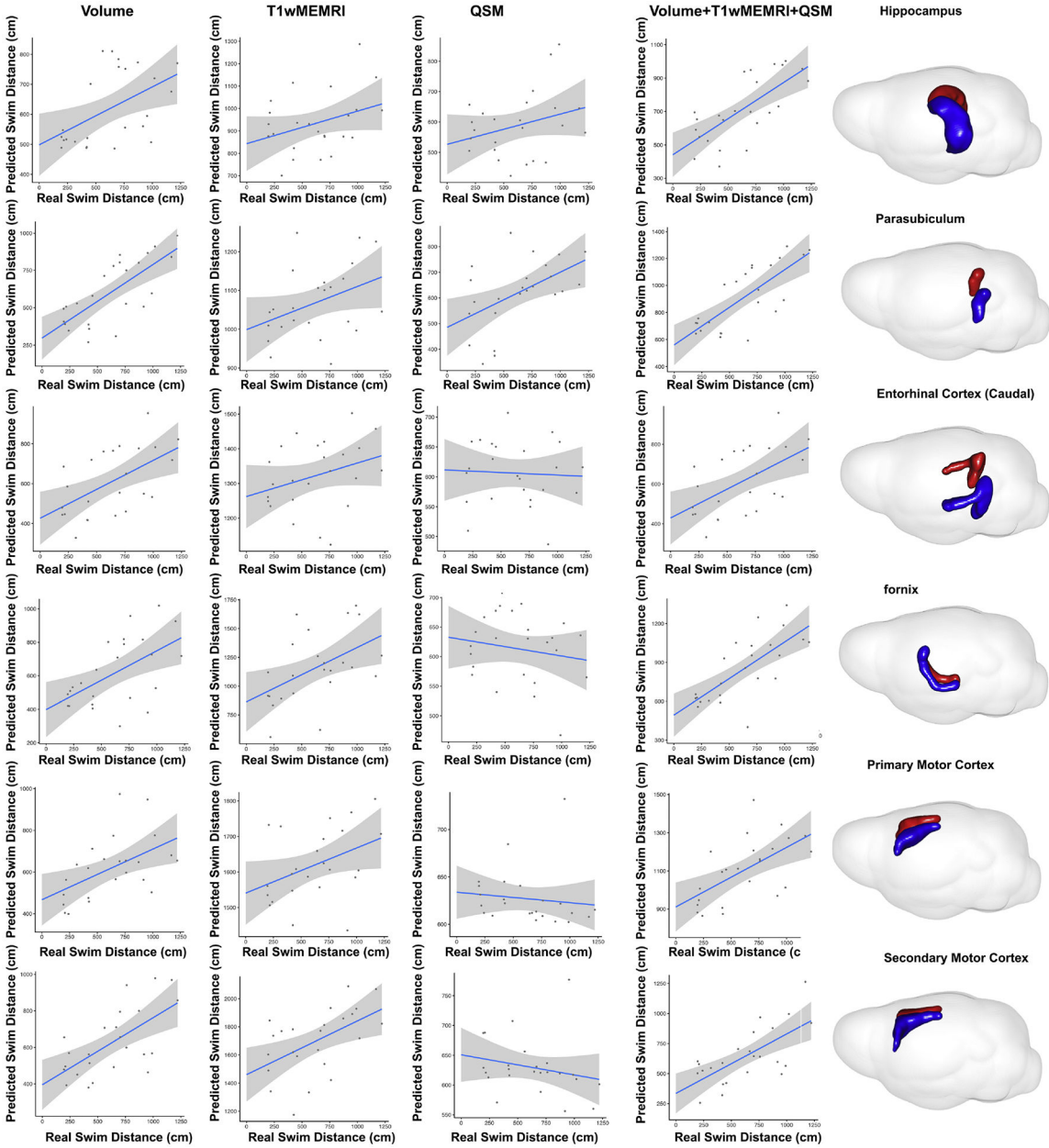

Figure 8: Relative to single biomarkers, the combined set of three contrasts performed in general better or just as well as the best predictor, in terms of the ability to predict swim distance for regions selected because they were *a priori* expected to be involved in memory or motor function, and/or AD pathology.

We note the good predictions for the parasubiculum, involved in spatial navigation.

Author Manuscript Author Manuscript Author Manuscript Author Manuscript

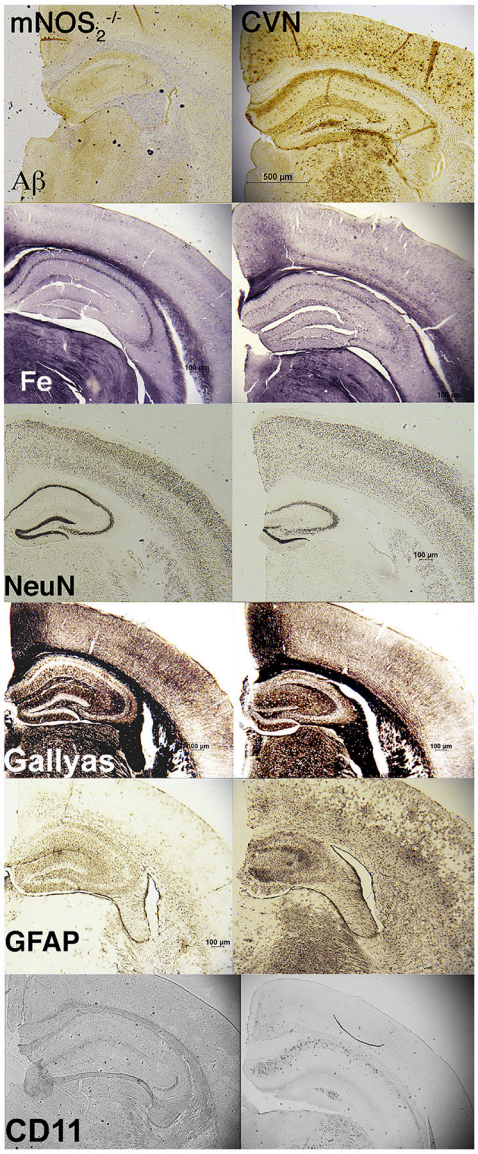

Figure 9: Histopathological correlates of imaging biomarkers in CVN-AD mice

included extracellular amyloid deposits, iron (ferritin), differential neuronal nuclei (NeuN) and myelin staining (Gallyas), as well as reactive astrocytes (GFAP) and activated microglia (CD11c). Amyloid beta deposition would lead to decrease in QSM in the hippocampus, and was also seen in the subiculum, and entorhinal cortex. However, our VBA results also identified QSM changes due to iron presence, in the hippocampus and in areas known to be rich in iron, such as the globus pallidus. These resulted in increased QSM in CVN-AD models. Reduction in myelination would lead to increased QSM, but the resolution of in vivo scan may not be sufficient to resolve such changes in small white matter tracts, however we observed such effects previously as well [76]. QSM changes do however overlap with areas of volume reduction, possibly associated with cellular density reduction (NeuN), leading to loss of anisotropy. The presence of reactive astrocytes and activated microglia may also result in microstructural changes, and possible damage to myelin.

Author Manuscript

Author Manuscript

Author Manuscript

Author Manuscript

Table 1.

Model performance comparison based on a whole brain unbiased analysis, showing the testing root mean square error of the predictions (RMSE); and the whole set based Pearson correlation (corr), associated p value, and the explained variance (adjusted R2).

Contrast	Model	Test RMSE test (cm)	P	CORR	adjR2	rank
VBA Volume	Positive Clusters	266.94±56.84	0.005	0.55	0.27	5
	Negative Clusters	259.33±57.20	0.004	0.57	0.3	3
	Combined Clusters	261.76±58.31	0.004	0.57	0.3	4
VBA T1wMEMRI	Positive Clusters	281.76±60.80	0.022	0.47	0.18	10
	Negative Clusters	273.98±54.30	0.01	0.51	0.23	7
	Combined Clusters	272.38±57.80	0.009	0.52	0.24	6
VBA QSM	Positive Clusters	285.55±73.88	0.036	0.43	0.15	11
	Negative Clusters	280.1±69.59	0.018	0.48	0.2	9
	Combined Clusters	290.6±50.53	0.01	0.52	0.23	12
Sparse Decomposition (SD)	Volume	300.7±48.89	0.021	0.47	0.18	14
	T1wMEMRI	344.54±41.26	0.12	0.33	0.07	15
	QSM	299.19±79.46	0.04	0.43	0.15	13
Supervised Sparse Decomposition (SSD)	Volume	251.05±68.81	3.43E-09	0.9	0.79	2
	T1wMEMRI	349.01±47.33	2.64E-07	0.84	0.69	16
	QSM	279±43.42	2.56E-05	0.75	0.54	8
Multivariate SSD	Volume+T1wMEMRI+QSM	233.08±101.78	7.14E-12	0.94	0.88	1

Author Manuscript Author Manuscript Author Manuscript Author Manuscript

Table 2.

Model performance comparison based on a ROI prior initialized based analysis, showing the testing root mean square error of the predictions (RMSE); and the whole set based Pearson correlation (corr), associated p value, and the explained variance (adjusted R2). Hc: hippocampus; PaS: parasubiculum; CEnt: caudal entorhinal cortex; fx: fornix; M1: primary motor cortex; M2: secondary motor cortex.

Contrast	Model	Test RMSE test (cm)	P	CORR	adjR2	rank
Hc	volume	288.57±93.68	0.013	0.50	0.22	7
	T1wMEMRI	332.1±38.63	0.0968	0.35	0.08	17
	QSM	332.51±34.31	0.1588	0.30	0.05	18
	combo	285.59±82.02	9.86E-05	0.71	0.48	6
PaS	volume	239.09±37.50	5.16E-05	0.73	0.51	1
	T1wMEMRI	334.78±27.95	0.0649	0.38	0.11	19
	QSM	283.29±90.10	0.0099	0.52	0.23	5
	combo	253.18±65.69	1.79E-05	0.76	0.55	2
CEnt	volume	268.77±60.51	0.0044	0.56	0.28	3
	T1wMEMRI	342.14±86.90	0.1402	0.31	0.06	21
	QSM	325.09±72.64	0.8108	0.05	0.04	16
	combo	322.26±108.69	0.0044	0.56	0.28	12
fx	volume	293.66±78.20	0.0062	0.54	0.26	8
	T1wMEMRI	350.61±103.41	0.1589	0.30	0.05	23
	QSM	339.23±69.64	0.0314	0.44	0.16	20
	combo	323.41±120.91	0.2297	0.25	0.02	13
M1	volume	323.83±131.29	0.0093	0.52	0.24	14
	T1wMEMRI	312.18±113.8	0.0501	0.40	0.13	10
	QSM	360.89±94.91	0.5723	0.12	0.03	24
	combo	317.01±162.54	0.0019	0.60	0.33	11
M2	volume	309.99±113.66	0.0008	0.64	0.38	9
	T1wMEMRI	276.51±56.14	0.0085	0.52	0.24	4
	QSM	342.94±87.03	0.2891	0.23	0.01	22
	combo	324.5±136.00	0.0003	0.68	0.44	15

Author Manuscript

Author Manuscript

Author Manuscript

Author Manuscript

Table 3.

To evaluate the 16 models performance, we have compared predictions with the true values for the measured behavior parameters (measured in cm) based on the full data set. Our Kruskall–Wallis analyses were followed by posthoc Tukey Kramer tests to control for the family wise error rate. Our results indicate that the supervised multivariate approach outperforms 12 of the other models. CI: confidence interval. VBA: voxel based analysis; SD2: supervised sparse decomposition.

Model1	Model2	CI1 (cm)	Difference (cm)	CI2 (cm)	p
T1wMEMRI_VBA−	COMBO_SSD	23.31	133.08	242.86	3.41E-03
COMBO_ SSD	VOLUME_SD	−237.98	−128.21	−18.43	0.01
T1wMEMRI_VBA+	COMBO_SSD	16.47	126.25	236.03	0.01
COMBO_ SSD	VOLUME_VBA+	−235.78	−126.00	−16.22	0.01
T1wMEMRI_VBA_COMBO	COMBO_SSD	14.72	124.50	234.28	0.01
QSM_VBA_COMBO	COMBO_SSD	14.72	124.50	234.28	0.01
COMBO_SSD	VOLUME_VBA−	−231.48	−121.71	−11.93	0.01
COMBO_ SSD	T1wMEMRI_SD	−229.15	−119.38	−9.60	0.02
COMBO_ SSD	VOLUME_VBA_COMBO	−227.65	−117.88	−8.10	0.02
COMBO_ SSD	VOLUME_SSD	−224.15	−114.38	−4.60	0.03
COMBO_ SSD	QSM_SSD	−223.57	−113.79	−4.02	0.03
COMBO_ SSD	T1wMEMRI_SSD	−222.03	−112.25	−2.47	0.04